POLITECNICO DI MILANO
DEPARTMENT OF ENERGY – NUCLEAR ENGINEERING DIVISION
DOCTORAL PROGRAMME IN ENERGY AND NUCLEAR SCIENCE AND TECHNOLOGY

SILICON MICRODOSIMETRY IN HADRON THERAPY FIELDS

Doctoral Dissertation of:
Eleni SAGIA

Supervisor:
Prof. Andrea POLA

Tutor:
Prof. Stefano AGOSTEO

The Chair of the Doctoral Program:
Prof. Carlo BOTTANI

XXVIII Cycle
2012 - 2015

Contents

INTRODUCTION 1
CHAPTER 1 3
Introduction to microdosimetry 3
1.1 Basic principles and microdosimetric quantities 4
1.2 Experimental methods in microdosimetry 6
1.3 Application of microdosimetry in hadron therapy 8
1.4 Standard techniques: uncertainties and limitations 9
CHAPTER 2 10
Silicon microdosimetry 10
2.1 A review of silicon devices for microdosimetry 11
2.2 Silicon microdosimeters: limitations and proposed corrections 11
2.2.1 Corrections for tissue equivalence 12
2.2.2 Corrections for shape equivalence 13
2.2.3 Charge collection confinement 14
2.2.4 Electronic noise 15
2.2.5 Angular response 15
CHAPTER 3 16
Silicon based solid state microdosimeters 16
3.1 The Monolithic Silicon Telescope (MST) Standard Prototype 17
3.2 The Segmented Monolithic Silicon Telescope (SMST) 18
3.3 The new experimental device 18
CHAPTER 4 19
Supplementary measurements with a 62 AMeV carbon ion beam at the CATANA facility 19
4.1 The CATANA facility 20
4.2 The irradiation set-up 20
4.3 Experimental results 21
CHAPTER 5 26
Characterization of a 290 AMeV carbon ion beam at the HIMAC facility 26
5.1 The HIMAC facility 27
5.2 The irradiation set-up 28
5.3 Experimental results 29
5.3.1 Irradiation of the monolithic silicon standard prototype (MST) with a clinical carbon ion beam 30
5.3.2 Irradiation of the segmented ΔE stage silicon device (SMST) with a clinical carbon ion beam 32
5.3.3 Irradiation of the monolithic silicon standard prototype (MST) with a pristine carbon ion beam 34
5.3.4 Revision of the experimental results 37

5.4 Experimental results and comparison with FLUKA simulations 39
CHAPTER 6 43
Preliminary measurements with a 362 AMeV clinical carbon ion beam at the CNAO facility 43
6.1 The CNAO facility 44
6.2 The irradiation set-up 45
6.3 Experimental results 47
6.4 Preliminary numerical study with the FLUKA Monte Carlo code 49
6.4.1 Simulation features 49
6.4.2 Simulation results 49
CHAPTER 7 54
Primary test of a monolithic silicon telescope with a 70 MeV carbon ion beam 54
7.1 The Australian National University Heavy Ion Accelerator Facility 55
7.2 The irradiation set-up 55
7.3 Experimental results 56
CONCLUSIONS 59
References 61

INTRODUCTION

Hadron therapy is one of the most sophisticated methods of radiation therapy that has been constantly evolving during the past decades. The use of hadron beams for cancer treatment can be more effective in comparison to the conventional radiotherapy, due to the high ballistic precision and the high biological effectiveness of the particles. The implementation of the hadron beams in cancer therapy raised the need of establishing protocols for the dosimetric characterization of the beams for therapeutic precision and radiation protection. Several attempts to provide standards and protocols for hadron therapy based on the conventional dosimetric approach were proved to be insufficient, since an average quantity such as the absorbed dose cannot provide information on the biological effects of the hadron beams that are strictly related to the local distribution of the energy deposited at micrometric scale. The microdosimetric approach of the characterization of hadron beams (Chapter 1) intends to cover this gap and provide information of all beam properties, both physical and biological.

Tissue–Equivalent Proportional Counters (TEPCs) are the main detectors used to perform microdosimetry for assessing the beam quality in hadron therapy. However, there are several problems and limitations in the use of TEPCs, such as distortions of microdosimetric distributions due to wall effects and paralyzation of the detector at high flux fields because of pile-up effects associated to high count rates. These drawbacks in addition to the lack of transportability and ease of use, mainly due to the need of a continuous tissue–equivalent gas flow system, encourage the seeking for alternative methods, such as silicon microdosimetry (Chapter 2).

A silicon microdosimeter, based on the monolithic silicon technology, was proposed during the past decade, by the Laboratory of Nuclear Measurements of "Politecnico di Milano" for hadron therapy applications. The device was irradiated with a 62 MeV clinical proton beam at the "Centro di AdroTerapia e Applicazioni Nucleari Avanzate" (CATANA) facility of the "Istituto Nazionale di Fisica Nucleare" (INFN) – "Laboratori Nazionali del Sud" (LNS) (Catania, Italy) and a 100 MeV pulsed proton beam at the Loma Linda University Medical Centre (California, USA). The results of these measurements confirmed the detector capability of characterizing a therapeutic proton beam. Preliminary measurements with a 62 AMeV carbon ion beam were also performed at the CATANA facility.

The aim of this thesis was to investigate the capability of characterizing a heavy ion beam with a silicon prototype device and its' geometrically varying versions (Chapter 3).

Supplementary measurements were carried out at the CATANA facility with a 62 AMeV carbon ion beam, under the same experimental conditions with the preliminary measurements performed in the past, in order to ensure reproducibility. Previous results were

used to compare and confirm the consistency of the new results and additional sets of measurements completed the characterization of this field (Chapter 4).

Chapter 5 presents the comparison of the numerical and experimental study carried out to characterize a 290 AMeV carbon ion beam at the Heavy Ion Medical Accelerator in Chiba (HIMAC) facility (Chiba, Japan). A comparison between the response of two different versions of the silicon device to the same field and a comparison of the detector response to two different fields (monoenergetic and clinical) of the same energy are also included.

Preliminary measurements aiming to demonstrate the silicon detector capability of characterizing a therapeutic carbon ion beam in comparison to the one of a TEPC were performed at the "Centro Nazionale di Adroterapia Oncologica" (CNAO) facility (Pavia, Italy) with a 362 AMeV clinical carbon ion beam (Chapter 6). Measurements were carried out with a mini – TEPC by INFN – "Laboratori Nazionali di Legnaro" (LNL), under the same experimental conditions, enabling the direct comparison of the results.

In seek of other potential microdosimetric applications of the silicon microdosimeter, its latest version was irradiated with a 70 MeV carbon ion beam in vacuum at the Heavy Ion Accelerator Facility of the Australian National University (Chapter 7). The device was irradiated for the first time in the context of an experiment aiming at better understanding the radiobiological effectiveness of a therapeutic carbon ion beam in the distal part of the Bragg peak and estimating the quality factor of carbon ions only with minimal fragment contribution.

CHAPTER 1

Introduction to microdosimetry

The patterns of the energy deposition process at micrometric scale are crucial for the understanding of the relative effectiveness of different kinds of ionizing radiation and the mechanisms of biological effect induction [1]. The limitation of macroscopic and average quantities, such as absorbed dose and LET to the specification of irradiation, without providing any information on the local energy distribution led to the inception of the field of microdosimetry [2].

The term of microdosimetry refers to "a conceptual framework and corresponding experimental methods for the systematic analysis of the microscopic distribution of energy deposition in irradiated matter" [3]. The fluctuations of energy deposited in individual cells and sub cellular structures and the microscopic tracks of charged particles are the subject of microdosimetry [4].

Microdosimetric concepts apply in various fields, such as radiation protection, radiobiology and dosimetry. The present work focuses specifically on microdosimetry as applied to hadron therapy.

The principle microdosimetric quantities are presented in this chapter. A brief review of the application of microdosimetry in hadron therapy fields is also included. Finally, the standard experimental microdosimetric techniques and their limitations are described.

1.1 Basic principles and microdosimetric quantities

Radiation has been used for therapeutic purposes soon after the discovery of x-rays in 1895 by Roentgen, on empirical basis since the mechanisms of radiation with matter were not known yet. The use of hadrons accelerated to high energies for treatment was firstly proposed by Robert Wilson in 1946, based on the mechanism interaction of protons with matter and specifically the dose increase at the end of the particle range forming the Bragg peak [5].

The first patient was treated with protons at the Lawrence Berkeley Laboratories in 1954, but only in 1986 the first hospital-based proton therapy facility, the Loma Linda University Medical Center became operational [6]. Ever since, the field of hadron therapy has been evolving constantly with many proton and carbon ion treatment facilities around the world. Hadron therapy is favored especially for the cases of deep seated and hypoxic tumors, since the high ballistic precision of hadrons spares critical organs near to the treating tumor from being irradiated and the radiation resistance due to the low oxygenation rate of the tumor is significantly lower for carbon ions.

The implementation of hadron beams in cancer therapy raised the need of establishing protocols for the dosimetric characterization of the beams for therapeutic precision and radiation protection. Several attempts to provide standards and protocols for hadron therapy based on the conventional dosimetric approach were proved to be insufficient, due to the limitations of the Linear Energy Transfer (LET) concept in explaining relative biological effectiveness (RBE) and the differences among radiation types.

The limitations of the LET rely on the fact that it is defined as an average over a large number of primary interactions, incapable of determining energy deposition in a small volume where for instance the mean number of interactions is one or less. In particular, particles with different charges and velocities can have the same LET, but it is the particle velocity that determines the energy distribution of the delta rays that is a major factor in the energy spatial distribution, especially at higher energy ions and small size sites. Moreover, the limited range of the particle relatively to the finite target is not considered by the concept of the LET. Such effects occur principally at lower energy ions and large size sites. Random fluctuations in energy deposition, such as clustering and straggling effects that are met at high energy ions and small size sites are neither taken into account by the concept of LET.

The insufficiency of the LET for providing any information on the local energy distribution led to the formulation of a set of measurable stochastic quantities that consist the basis of the field of microdosimetry that raised from the study of radiation effects on living cells.

The basic quantity is the energy deposit ε_i that is defined as the energy deposited in a single interaction i:

$$\varepsilon_i = T_{in} - T_{out} + Q_{\Delta m}$$

where T_{in} and T_{out} are the energies of the incident ionizing particle and the sum of the energies of all ionizing particles leaving the interaction (excluding the rest mass), respectively. $Q_{\Delta m}$ are the changes of the rest mass energy of the atom and all particles involved in the reaction.

The energy imparted ε to the matter in a volume is the stochastic quantity

$$\varepsilon = \sum_i \varepsilon_i$$

the sum of all energy deposits ε_i in the volume, due to one or more energy deposition events.

The principle microdosimetric quantities are the specific energy z and the lineal energy y that have been defined formally by the International Commission on Radiation Units and Measurements (ICRU, 1980) [7], as following:

The quotient of ε by m, where ε is the energy imparted in any number of events and m is the mass of the matter in a volume, gives the specific imparted energy z:

$$z = \frac{\varepsilon}{m}.$$

The measurement unit is gray (Gy), where 1 Gy = 1 J/kg.

The quotient of ε to $\bar{l}$, where $\bar{l}$ is the mean chord length of the considered volume, gives the linear energy y:

$$y = \frac{\varepsilon}{\bar{l}}.$$

The unit of the quantity is J/m, but it is most commonly expressed in keV/μm. It should be stressed that in the definition of the lineal energy, the energy imparted ε refers to a single event. As mean chord length is defined the mean length of randomly oriented chords in a volume and for a convex body is calculated by Cauchy's theorem $\bar{l} = 4 \cdot V/A$, where V is the volume and A is the surface area of the body.

The mean values of the frequency distributions of z and y have been defined for specific applications. The mean specific energy is

$$\bar{z} = \int_0^\infty z \cdot f(z)\, dz$$

where $f(z)$ is the probability density distribution. The mean specific energy $\bar{z}$ is a non-stochastic quantity and is usually equal to absorbed dose D. This relies on the fact that microdosimetry concerns mainly volumes sufficiently small that the dose in most types of irradiation can be considered to be constant. Since $\bar{z} = D$, the integrand $z \cdot f(z)$ is the contribution to the dose delivered between z and $z + dz$. So, the dose distribution of z is considered to be

$$d(z) = \frac{z \cdot f(z)}{\bar{z}}.$$

Thus, by averaging $f(z)$ and $\mathrm{d}(z)$, the frequency mean specific energy $\overline{z_F}$ and the dose mean specific energy $\overline{z_D}$ are derived, respectively. Accordingly, the frequency mean lineal energy $\overline{y_F}$ and the dose mean lineal energy $\overline{y_D}$ are derived.

Due to the wide range of the microdosimetric distributions values, microdosimetric spectra are typically represented semi-logarithmically. Specifically, lineal energy distributions are represented as $y \cdot f(y)$ vs $log(y)$ plots, while dose distributions $y \cdot d(y)$ vs $log(y)$, preserving the probabilistic meaning of the areas displayed in the spectra.

1.2 Experimental methods in microdosimetry

The objective of the experimental microdosimetry is to measure the microdosimetric quantities in well-defined volumes. The use of low-pressure proportional counters for microdosimetric measurements was initially introduced by Rossi in the early 1950s, permitting measurements at the scale of the order of 1 μm, based on the principle of simulation of solid microdosimetric volumes by geometrically similar gas volumes of equal effective dimensions by changing the gas density. Figure 1.1 shows a spherical Rossi chamber that was actually used by Rossi at Columbia University [8].

The proportional counters for microdosimetric use contain tissue-equivalent gas (propane or methane based) and have tissue-equivalent plastic walls. In order to preserve the secondary particle fluence independent of density, the atomic composition of the wall and gas must be identical, according to Fano's theorem [9]. This requisite does not always apply in practice. Neither does the condition of density independent mass stopping power, due to polarization effects in solids induced by relativistic charged particles [10]. Furthermore, the density difference between the cavity and the surrounding walls can induce distortions to the microdosimetric distributions acquired [11]. "Wall effects" arise due to the fact that the energy is not deposited along straight lines, as particles may scatter and their tracks may generate branches of secondaries and tertiaries. Therefore, wall effects can also occur even if the filling gas and the counter walls are of the same composition. An analytical assessment of errors introduced by wall effects in microdosimetric measurements was conducted by Kellerer [12] and the use of wall-less counters was proposed for the elimination of the errors.

Figure 1.1: A spherical Rossi counter that was actually used by Rossi at Columbia University [8].

Despite these issues, the tissue-equivalent proportional counters (TEPCs) are the main instruments for microdosimetric measurements. TEPCs consist of a spherical or cylindrical gas chamber equipped with a central anode wire electrically isolated from the surrounding chamber walls. A voltage is applied between the anode and the conductive wall so that the ions created by the irradiation drift along the electric field lines. The amount of the collected charge represents the number of the ion pairs produced and if the average energy required for an ion pair production is known, the energy deposited within the chamber volume can be estimated [13].

The atomic composition of the filling gas is crucial for the quality of the measurement. However, the gas purity is hard to be preserve due to its absorption by the chamber walls and the release of electronegative gases. The use of a gas flow system prevents these effects, but complicates the measurement procedure. Thus, usually it is avoided and the use of the detector in sealed mode for days or even weeks with continuous maintenances is preferred.

The simulation of even smaller microdosimetric volumes that would reach the nanometric scale led to the development of the miniaturized TEPCs, a low pressure cylindrical proportional counter with miniaturized dimensions of all components. The prototype succeeded in measuring single event energy deposition spectra at 5 nm to 250 nm simulated site sizes [14]. Mini-TEPCs capable of simulating sites down to about 300 nm were designed and constructed

at the INFN National Legnaro Laboratories in order to facilitate microdosimetric measurements in high-flux fields, since the pile-up effects due to the high count rates are limited [15]. Therefore, detectors of sensitive volume less than 1 mm^3 are preferred for realistic microdosimetric characterization of hadron therapy fields [16].

1.3 Application of microdosimetry in hadron therapy

Linking the physical parameters to the biological effects of the radiation is one of the main challenges in the field of radiation therapy and more particularly in hadron therapy.

The concept of the relative biological effectiveness (RBE) was introduced considering the divergence in the effect of radiations of different type for the same physical dose. In conventional radiotherapy, the RBE does not vary significantly for photons and electrons within the energy ranges used in therapy and is independent from the position within the tissue. On the contrary, RBE values for heavier particles vary remarkably with several parameters such as depth, type and energy of radiation, biological end point, dose fractionation history and cell line [17].

The applied RBE in clinics defines the effective dose delivered on the patient and consequently the high accuracy of the values is crucial for the optimization of the treatment. For proton treatment, the RBE value is considered to be constant and equal to 1.1, disregarding the dependencies on physical and biological properties based on the fact that the magnitude of the RBE variations is relatively small (within 10-20%) in the plateau region of the SOBP, while differences are much higher in the distal edge [18]. For heavier ions though, the RBE varies widely with depth with the highest values found at the end of the range of the ions, where the high local ionization density causes clustered lesions producing irreparable DNA damage [19]. Therefore, different radiobiological models are currently used for the prediction of the RBE values in carbon ion therapy.

The clinical RBE of the carbon ion beams that is applied at the Heavy Ion Medical Accelerator in Chiba (HIMAC) facility (Chiba, Japan) was determined empirically based on the clinical experience with fast neutron beams of the National Institute of Radiological Sciences (NIRS) and a dose-scaling procedure. However, the method considers only the LET dependency of the RBE without taking into account the dose and the radio sensitivity of the irradiated tissues [20].

A track structure based model was developed at the GSI Helmholtz Center for Heavy Ion Research (Darmstadt, Germany) for the RBE estimation based on the dose profile pf the incident primary particle, the target geometry and the photon survival curves [21]. The Local Effect Model (LEM) has been implemented in commercially available treatment planning systems and has also been adopted by the Heidelberg Ion Beam Therapy Center (HIT) (Heidelberg, Germany) and the “Centro Nazionale di Adroterapia Oncologica” (CNAO) facility (Pavia, Italy). The drawback of this approach relies on the assumption that the low-LET survival curve (photon) can be used to characterize the effect of high-LET radiation, despite the experimental observations.

Since these methods of RBE calculation are prone to uncertainties, based on approximations and assumptions due to the large number of parameters involved, a microdosimetric approach for hadron beams was proposed in the literature during the last decade. Microdosimetric methods provide the detailed knowledge of the local energy distribution of the therapeutic beam that can be correlated with radiobiological data for the specification of the radiation quality. In particular, the radiation quality is estimated through the dose probability density $d(y)$ and the dose mean lineal energy $\overline{y_D}$.

A method for beam quality assessment in terms of RBE based on the convolution of microdosimetric distributions with a biological weighting function $r(y)$ was firstly proposed by Wambersie [22]:

$$RBE_{\mu} = \int_0^{\infty} r(y) \cdot d(y) \cdot dy.$$

The weighting function $r(y)$ must be derived by performing in parallel microdosimetric and radiobiological measurements of a specific radiation field, since the radiobiological effects depend on several parameters, as listed above. Several biological weighting functions have been calculated for various cases and are available in literature [23- 25].

The RBE_{μ} value estimated through this procedure is called microdosimetric calculated RBE and is valid only for the conditions at which the biological weighting function was derived.

Numerous microdosimetric proton beam characterizations have been carried out at different facilities around the world and demonstrate the inaccuracy of the assumption of a constant clinical RBE value [26-28]. Similar studies were presented recently for carbon ion therapeutic fields, where microdosimetric measurements were performed with TEPCs and ΔE-TOF (Time of Flight) scintillator based technique [29-32].

1.4 Standard techniques: uncertainties and limitations

The standard microdosimetric techniques imply the use of TEPCs for the estimation of beam quality, while the mini-TEPCs are regarded as the reference detectors for the applications in hadron therapy. TEPCs are the most appropriate devices for microdosimetric measurements due to their response that is accurate over a wide energy range, in particular with high sensitivity to low energy particles and independent of the characteristics of the radiation field, as energy and particle LET. Also, the sensitive volume is well defined, tissue-equivalence is achieved and a wide range of site dimensions can be simulated, providing the ability to measure single event spectra on nanometric level [33].

However, the need of a continuous tissue–equivalent gas flow system induces practical difficulties and additional costs in the management and the maintenance of the detection system. The complexity in use, lack of transportability and high cost, in addition to low spatial resolution, wall and density effects (section 1.2) encourage the seeking of alternative methods, such as solid state microdosimetry.

CHAPTER 2

Silicon microdosimetry

Silicon microdosimetry seems to be a potential candidate for clinical quality assessment in hadron therapy, since it can provide user friendly, low cost and technologically consolidated services. However, there are some open issues concerning the use of silicon devices, such as the tissue equivalence, the charge collection confinement, the shape and the dimensions of the detectors' sensitive area and the electronic noise that defines the minimum detectable energy. There are several proposals for facing these issues, but further studies are required in order to optimize the proposed solutions that can also vary for different detectors.

A brief review of the development of solid state microdosimetry is presented in this chapter. The essential limitations of the silicon microdosimeters are explained and corrections proposed in the literature are also described.

2.1 A review of silicon devices for microdosimetry

The limitations of the TEPCs raise the need of alternative methods for performing microdosimetric measurements. Solid state microdosimeters based on silicon devices seem to be promising, especially due to the low cost and easy accessible silicon technology.

The study of semiconductor solid state detectors for microdosimetric applications dates back to 1980, when an extensive comparison of microdosimetric measurements between a single junction solid-state detector and a spherical proportional counter in a range-modulated negative pion field was carried out [34]. The discrepancies were attributed mainly to the dimensions of the sensitive volume of the silicon detector, by Monte Carlo calculations. More specifically, the relatively large sensitive thickness of the silicon detector permitted a significant fraction of heavy ion stoppers. Also, conventional algorithms used to unfold LET distributions from the silicon detector data were proved to be insufficient because of the large fraction of events from particles that start and stop in the detector.

Since then, several systems based on single silicon photodiodes were investigated for their ability of performing microdosimetric measurements in various fields, such as cosmic radiation and radiation protection [35-37]. Similarly, the differences that occur in the comparison of the silicon systems with the TEPCs were also attributed to the shape and dimensions of the sensitive volumes. Attempts at developing silicon microdosimeters based on arrayed diode devices, due to the low efficiency of a single diode, in order to maximize counting statistics, are also available in the literature [38]. Towards this direction, a silicon microdosimeter prototype consisting of a diode array of microscopic p-n junctions based on silicon-on-insulator (SOI) technology was developed and tested in different hadron therapy fields [39, 40]. The development of this detector is remarkable because the sensitive volume of the detector is well confined and the "field funneling effect", one of the main drawbacks in silicon microdosimetry, is minimized, due to the presence of a SiO_2 insulator.

One of the most recent devices proposed for silicon microdosimetry in hadron therapy applications is the Monolithic Silicon Telescope, which allows not only to minimize the field funneling effect, but also to optimize the microdosimetric measurements by providing information about the energy and type of the interacting particles [41]. The performance of the prototype device and its' successors in hadron therapy fields is the subject of this work.

2.2 Silicon microdosimeters: limitations and proposed corrections

Silicon devices can be an asset for microdosimetry, not only based on practical criteria as the ease of use and technological accessibility, but also for their performance. The most significant feature of silicon detectors is the possibility of constructing devices of micrometric dimensions. Thus, physical events can be measured in an actual micrometric site in contrast to the TEPCs that the dimensions of the site are simulated. Energy resolution depends on the silicon device capacitance and on the preamplifier noise. Therefore, silicon microdosimeters have lower energy sensitivity than the TEPCs, which are even capable of single ionization detection, due to

silicon detectors' higher noise. Yet, at higher energies the theoretical contributions to the energy resolution, as the Fano factor and gas multiplication are dominant, while the preamplifier noise is a less significant component. Consequently, silicon microdosimeters have better resolution at higher energies since their theoretical contributions (lower Fano factor, no gas multiplication) are lower than the ones of the TEPCs.

The excellent spatial resolution, in combination with the capability of in-vivo operation and pile-up robustness, make silicon detectors remarkably adequate for hadron therapy applications. In addition, their compactness, low cost, ability of multiple shape manufacturing, transportability, low power consumption and low sensitivity to vibrations make silicon devices a viable alternative to the TEPCs. Nevertheless, there are some issues concerning the use of silicon devices that need to be solved, such as the tissue equivalence, sensitive volume definition, charge collection confinement, electronic noise and angular response.

2.2.1 Corrections for tissue equivalence

In solid state microdosimetry, microdosimetric spectra are acquired in silicon and have to be corrected for tissue equivalence. A tissue equivalent converter is required on the top of the silicon devices when measurements are performed outside a tissue equivalent phantom. Ideally, all secondary particles that are produced by particles that interact directly with silicon should be absent, or at least should have a negligible contribution with respect to those generated in the tissue equivalent area that should precede the detector. Also, it is important that among the particles that interact with the micrometric sensitive volume only "stoppers" (particles generated outside the volume and completely stopped within it) and "crossers" (particles produced outside the volume which cross it) should be taken into account, while "insiders" (particles stopped within the volume) and "starters" (particles that leave the volume before completely depose their energy) must be minimized.

The amount of the energy imparted by stoppers within the sensitive volume can be considered to be independent of the detector material (apart from border effects) since for these particles the detector can be considered as an absorber of infinite thickness.

On the contrary, the energy imparted by crossers in the silicon detector must be corrected for tissue-equivalence. This can be done by scaling the energy imparted in silicon ε_{Si} with the ratio R,

$$R = \frac{S^{Tissue}(E)}{S^{Si}(E)},$$

where $S^{Tissue}(E)$ and $S^{Si}(E)$ are the stopping power of the impinging particle of energy E in tissue and in silicon, respectively [42]. Hence, the energy imparted in an analogous tissue equivalent detector $\varepsilon_{STissue}$ is calculated by the following expression:

$$\varepsilon_{Tissue} = \varepsilon_{Si} \cdot R(E) = \varepsilon_{Si} \cdot \frac{S^{Tissue}(E)}{S^{Si}(E)}.$$

The ratio $R(E)$ clearly depends on the energy of the impinging particle. In the cases that this information is missing, an approximate correction is applied by using an average correction factor ζ given by the following expression:

$$\zeta = \frac{\int_{E_{min}}^{E_{max}} R(E)dE}{E_{max} - E_{min}} = \frac{\int_{E_{min}}^{E_{max}} \frac{S^{Tissue}(E)}{S^{Si}(E)} dE}{E_{max} - E_{min}}$$

where E_{min} and E_{max} are the minimum and maximum limit of the energy range of the impinging particles, respectively. Consequently, in the cases that the particle energy E cannot be assessed, the energy $\varepsilon_{STissue}$ is scaled with the constant factor ζ:

$$\varepsilon_{Tissue} = \varepsilon_{Si} \cdot \zeta.$$

For future reference, it should be mentioned that in the current work, the tissue equivalent correction procedure that was followed consists in correcting event-by-event the energy ε_{Si}, as permitted by the detectors that were used.

2.2.2 Corrections for shape equivalence

The capability of the silicon devices as microdosimeters can be demonstrated by comparing them to the reference microdosimeters, the TEPCs. TEPCs are spherical, while silicon detectors are usually structures with plane surfaces, such as rectangular parallelepipeds, due to the silicon integrated circuit technology that is based on planar lithographic processes. Therefore, this comparison requires an additional correction of the acquired microdosimetric spectra that takes into account the differences in shape of the sensitive volume of both devices. The shape equivalence is based on the parametric criteria given in the literature [43, 44] and based on the dose-mean energy imparted per event $\bar{\varepsilon}_D$:

$$\bar{\varepsilon}_D = \frac{\int_0^\infty \varepsilon^2 \cdot p(\varepsilon) \cdot d\varepsilon}{\int_0^\infty \varepsilon \cdot p(\varepsilon) \cdot d\varepsilon}$$

where $p(\varepsilon)$ is the frequency distribution of the imparted energy ε to the sensitive volume of interest.

By assuming a particle crossing a sensitive volume with a chord length distribution $p(l)$ and a constant linear energy transfer L, the dose-mean energy imparted per event $\bar{\varepsilon}_D$ equals to the product of L that is the energy deposited per unit length and the mean cord length $\bar{l}$ and is given by the following expression:

$$\bar{\varepsilon}_D = L \cdot \frac{\int_0^\infty l^2 \cdot p(l)\, dl}{\bar{l}} = L \cdot \bar{l}.$$

By equating the dose-mean energy imparted per event for the two differently shaped devices considered

$$\bar{\varepsilon}_{D(Si)} = L \cdot \bar{l}_{D(Si)}$$

and

$$\bar{\varepsilon}_{D(TEPC)} = L \cdot \bar{l}_{D(TEPC)},$$

so, the shape-correction factor can be defined as

$$\eta = \frac{\bar{l}_{D(TEPC)}}{\bar{l}_{D(Si)}}.$$

Therefore, the value of η is the scaling factor that can be applied to the mean cord length $\bar{l}$ of the silicon device in order to obtain a mean cord length $\bar{l}_{eq}$ equivalent to that of the reference microdosimeter,

$$\bar{l}_{eq} = \eta \cdot \bar{l}.$$

2.2.3 Charge collection confinement

One of the most important requirements in microdosimetry is the well-defined sensitive volume of the detector. However, this condition cannot be easily fulfilled due to the complexity of the charge collection process.

Charges are not only collected via drift in the depletion region, as expected based on the basic principles of semiconductor detectors. Instead, charge collected via diffusion from outside of the depletion region may contribute significantly to the charge collection. Diffusion effects can be occurred by random thermal motion due to a gradient of carrier concentration.

The field funneling effect is another phenomenon that can lead to false charge collection [45]. This effect occurs due to local distortion of the electric field, induced by high-LET particles in the depletion layer, resulting to charge collection from the non-depleted zone. Consequently, the thickness of the sensitive zone of the detector depends on the LET and the sensitive volume cannot be defined, resulting insufficiency of the detector to operate as a microdosimeter. Therefore, lateral diffusion and charge sharing effects, including the field funneling effect should be minimized.

The field funneling effect was firstly observed in PIN diodes. The strong presence of the effect and its impact on its performance led to the conclusion that the detector cannot be considered for microdosimetric use and the need of minimizing the field funneling effect became a priority in the future evolvement of the solid state microdosimetry. Typical examples of detectors that have managed to minimize the field funneling effect are SOI technology prototype microdosimeter and the monolithic silicon telescope, as already mentioned (section 2.1).

Additionally to these effects, the moderate radiation hardness of silicon devices can affect the charge collection process. In particular, high energy radiation may interact with semiconductor materials producing defect complexes that reduce the charge collection efficiency by reducing the minority carrier lifetime, mobility and by changing the majority carrier density.

2.2.4 Electronic noise

The electronic systems that are used for signal acquisition during microdosimetric measurements are relatively similar, regardless the type of detector. However, the lack of any internal gain (i.e.: gas multiplication in TEPCs) in silicon microdosimeters requires the use of a preamplifier. This affects the detector performance by defining the threshold of the low energy sensitivity.

Semiconductor devices are characterized by thin depletion regions (of about a few micrometers). The thickness of the depletion layer w_{dl} can be calculated from the following expression:

$$w_{dl} = \frac{\varepsilon_{Si}}{C_{det}}$$

where ε_{Si} is the dielectric constant of silicon (~ 1.04 pF·cm^{-1}) and C_{det} the specific capacitance of the detector. Consequently, the thin depletion regions dictate high values of specific capacitance of the detector that result high electronic noise and thus high limit of minimum detectable energy.

A representative example is the silicon devices that were used in the present work with a depletion region of about 1 μm in thickness a capacitance of about 100 pF. Such high capacitance limits the minimum detectable energy to about tenths of keV, while for a TEPC this is fractions of keV.

2.2.5 Angular response

The response of silicon devices present an angular dependency in contrast to the TEPCs that show isotropic angular response. Most silicon devices consist of plane surfaces with different structures includes, so the geometry of the interaction and accordingly the track length distributions change with the angle of the incident beam.

Therefore, irradiation conditions should be evaluated carefully, in order to minimize the angular dependence of the response. For instance, in the present study the detectors were placed vertically to the incident beam, with the ΔE stage preceding E stage, as indicated by the working principles of the detector.

CHAPTER 3

Silicon based solid state microdosimeters

Since the last three decades, silicon microdosimeters are being studied as they can offer sensitive zones of micrometric dimensions. Towards this direction, an innovative silicon device has been proposed for microdosimetric applications by the group of Nuclear Measurements of "Politecnico di Milano".

The detector is based on the monolithic silicon telescope technology that produces micrometric monolithic structures with two stages made out of a single silicon wafer by exploiting deep ion implantation through high energy boron ions [46, 47]. A pixelated version, also mentioned as segmented, has followed the prototype device [48] and a successor of the device has been developed recently, but refinement is still ongoing.

All devices, fabricated by ST-Microelectronics (Catania, Italy), were used in experimental campaigns that are outlined in the present thesis. A description of the detectors' geometry is included in this chapter.

3.1 The Monolithic Silicon Telescope (MST) Standard Prototype

The first configuration of the telescope device that was considered for microdosimetry consists of a surface ΔE stage, about 1.9 μm in thickness coupled to a residual energy E stage, about 500 μm in thickness (Figure 3.1). The two stages are made out of a single silicon wafer and share a p+ well generated through high energy ion implantation. In such way, the ΔE stage is well confined, the edge fluctuations are limited and thus the "field funneling effect" is minimized.

The ΔE stage acts as a microdosimeter (single ΔE-element microdosimeter), while the residual energy E stage provides information on the energy and type of the incident radiation and allows optimized energy dependent corrections for tissue-equivalence to be performed event-by-event. This feature is fundamental since it enables the comparison of the microdosimetric spectra acquired with the silicon device to the ones acquired with a tissue-equivalent proportional counter.

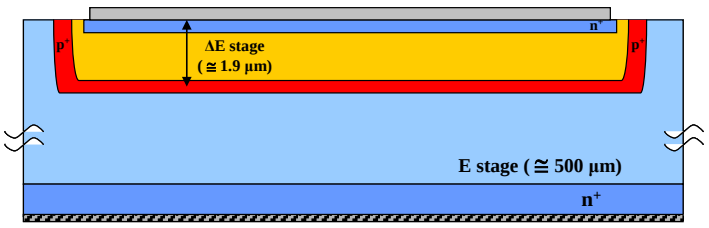

Figure 3.1: A schematic view of the monolithic silicon telescope. The detector consists of a ΔE stage (about 1.9μm of thickness) implanted on a single E stage (500 μm thick).

3.2 The Segmented Monolithic Silicon Telescope (SMST)

A telescope device with a ΔE detector geometrically segmented in micrometric cylinders was also developed in order to provide sensitive volume dimensions similar to those which can be simulated by a tissue-equivalent proportional counter (figure 3.2).

This pixelated version consists of a matrix of micrometric cylindrical diodes ΔE elements, about 2 μm in thickness and 9 μm in diameter) coupled to a single residual energy E stage, about 500 μm in thickness. More than 7000 of ΔE elements are electrically connected in parallel, giving rise to a single ΔE surface stage of the desired active area of about 0.5 mm^2. Each ΔE element is surrounded by a guard-ring 14 μm in diameter that confines charge collection within the lateral surface of the sensitive volume and acts as a solid-state microdosimeter, while the residual energy of the impinging particle is measured by the E stage.

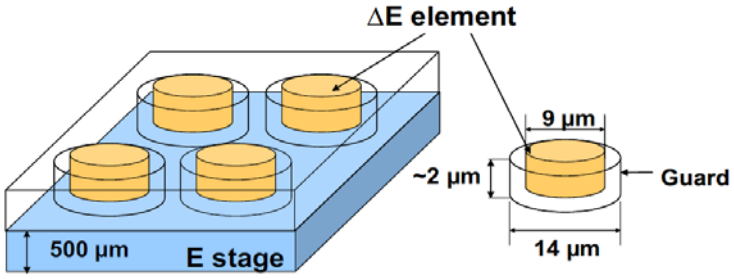

Figure 3.2: Sketch of the pixelated silicon telescope. The detector consists of a matrix of cylindrical ΔE elements (about 2 μm in thickness and 9 μm in diameter) implanted on a single E stage (500 μm thick). ΔE element surrounded by a guard of 14 μm in diameter. More than 7000 ΔE elements are connected in parallel to give an effective detection area of about 0.5 mm^2.

3.3 The new experimental device

The new device differs from the previous versions in both the design and the production process. More specifically, the new detector consists of a ΔE and an E_{tot} stage, about 2 μm and 700 μm in thickness, respectively, providing a circular sensitive area of 1 mm^2. Additional p+ guards were implemented in order to better define the active area and further reduce the "field funneling effect" and charge diffusion. Also, the doping materials were changed and the technology of the boron implantation procedure was modified.

The refinement of the device is still ongoing and the design and details of the production procedure will be published near in the future by ST-Microelectonics.

CHAPTER 4

Supplementary measurements with a 62 AMeV carbon ion beam at the CATANA facility

The response of the solid state microdosimeters to proton beams has been studied and an extensive characterization of a 62 MeV clinical proton beam at the CATANA facility has been carried out in the past [49]. The subject of this research activity is to proceed with the study of the response of the detectors to carbon ion beams and the characterization of clinical carbon ion fields.

This experimental activity is supplementary to preliminary measurements that had been performed during the first attempt of irradiating the detectors with a carbon ion beam [50]. A segmented silicon telescope was irradiated with a 62 AMeV (MeV per nucleon) carbon ion beam for different points along the Bragg peak inside a PolyMethyl MethAcrylate (PMMA) phantom [51].

4.1 The CATANA facility

The “Centro di AdroTerapia e Applicazioni Nucleari Avanzate” (CATANA) has been built at the “Laboratori Nazionali del Sud” (LNS) of the “Istituto Nazionale di Fisica Nucleare” (INFN) in Catania (Italy) in collaboration with the University of Catania and is the first Italian protontherapy facility. Since 2002, proton radiation treatment has been available at the CATANA facility for the treatment of eye lesions, as choroidal and iris melanoma. After 10 years of activity, about 300 patients had been treated at the facility.

The treatment of eye tumors (4 cm maximum) is performed with a 62 MeV proton beam delivered by a superconducting cyclotron and the beam delivery system is passive. The beam exits in air through a 50 μm kapton window located at about 3 m from the isocenter. Before the exit window, a tantalum scattering foil of 15 μm is placed in vacuum. After the exit of the beam by the window, there is a second tantalum foil of 25 μm provided with a central brass cylinder of 4 mm in diameter. The double foils provide beam homogeneity in terms of lateral off-axis dose distribution, minimizing the energy loss [52]. A PMMA range shifter degrades the beam energy to the appropriate value that corresponds to the desired depth, where the tumor is seated and a PMMA wheel modulated the energy of the beam and forms the Spread-Out Bragg peak. Also, a transmission Monitor Chamber is implemented in the treatment line in order to control online the active dose delivered to the patients.

The purpose of the CATANA since the beginning has been the application of eye proton therapy, but also the research activity. Different dosimetric systems for absolute and relative dosimetry have been characterized, studied and developed, in order to achieve accuracy in dose delivery [53]. A parallel-plate Markus Ionization Chamber has been set as the reference detector for the absolute dose measurement.

4.2 The irradiation set-up

A pixelated silicon telescope (SMST) was placed inside a PMMA phantom at different depths and irradiated with a 62 AMeV carbon ion beam. The irradiation field is not clinical, however serves the purpose of testing the detector response to carbon ion beams.

The measurements were performed at the “Test facility”, where the primary beam was extracted through a kapton window after passing through a 15 μm tantalum scattering foil. A range shifter, a monitor chamber and a brass collimator were used to shape and monitor the beam. Figure 4.1 is a picture of the irradiation set-up and the beam delivery line.

Figure 4.1: A picture of the irradiation set-up and the beam delivery system of the "Test" experimental room of CATANA facility.

PMMA foils of different thicknesses (50 μm, 2.5 mm and 3 mm) were placed in front of the detector in order to change the detector position across the Bragg peak. The thickness uncertainty was estimated at about 0.2 mm.

A custom configuration of electronics including chip preamplifiers and amplifiers for the signals acquired was used, while for the preliminary measurements the acquisition was performed by a custom two-channel ADC in coincidence mode, in order to maintain the time correlation.

4.3 Experimental results

Since the aim of the experimental campaign was to verify and conclude the results of the first attempt of irradiation of the silicon microdosimeter with carbon ion beam, the measurements were carried out at the same experimental site and under the same experimental conditions. The geometrical and tissue equivalence corrections were also performed following the same procedures as the preliminary measurements: mean chord length was considered to be 1.522 μm and the tissue equivalence of silicon was performed by measuring event-by-event the energy of the impinging particles.

Some measurement points were common (7.5 mm, 7.6 mm, 7.65 mm, 7.7 mm and 8 mm in depth) in order to verify the reproducibility of the measurements. The scatter plots of the energy imparted per event in the ΔE stage versus that deposited in the E stage, for the same measurement points across the Bragg peak (excluding 8 mm that is located beyond the Bragg peak) are shown in figures 4.2 (a) – (d). Figure 4.3 shows the lineal energy distributions acquired for these points.

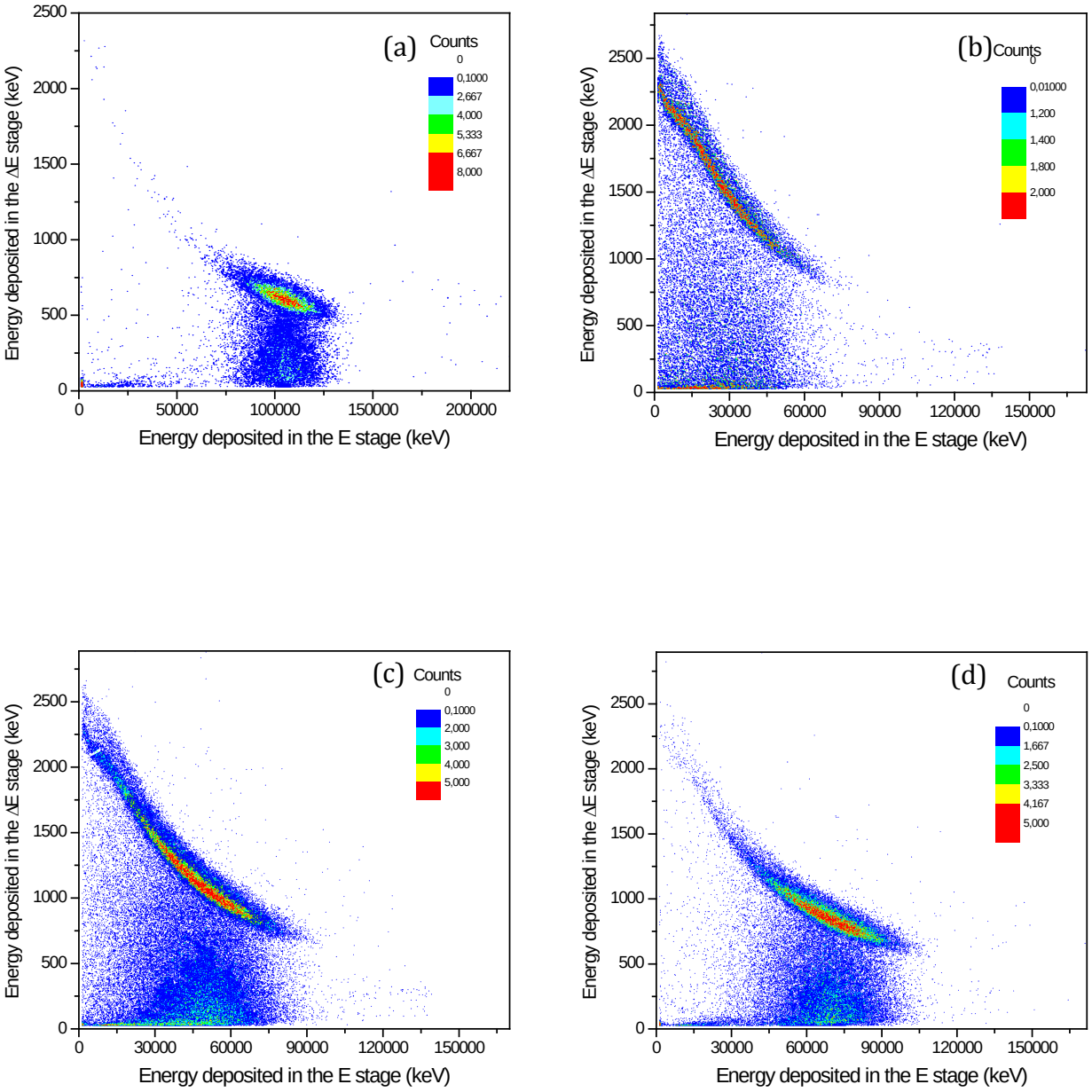

Figure 4.2: ΔE-E scatter plots measured across the Bragg peak, at the phantom depth of (a) 7.5 cm, (b) 7.6 cm, (c) 7.65 cm and (d) 7.7 cm.

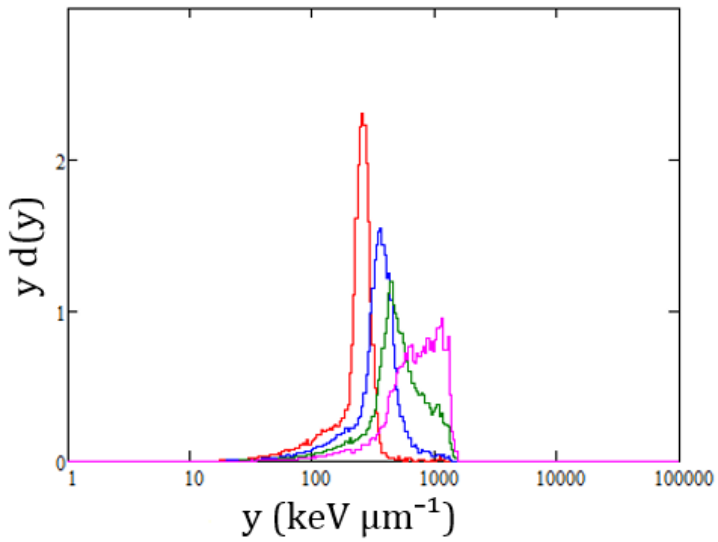

Figure 4.3: Lineal energy spectra obtained with the pixelated silicon microdosimeter at PMMA depths of 7.5 mm (red curve), 7.6 mm (blue curve), 7.65 mm (green curve) and 7.7 mm (pink curve), corrected adequately.

Microdosimetric data were also acquired at depths that correspond to the fall off region of the Bragg peak (7.7 mm-8 mm) with a step of 50 μm. Figure 4.4 (a) – (d) show the scatter plots of the energy deposited for the points 7.7 mm-7.85 mm (with a step of 50 μm) of this interval located across the Bragg peak, where major shifts in the spectra can be noticed. The analytical responses to the ions, from hydrogen to carbon are also included [54]. In particular, the orange curve corresponds to the analytical distribution of the carbon ions, while the rest of the curves refer to the fragments distributions: boron (red curve), beryllium (pink curve), lithium (green curve), helium (black curve) and hydrogen (purple curve). Therefore, the different fragment contributions are easily identified. For instance, in figures 4.4 (c) and (d) there is not any contribution from the primary beam and only fragments are present. Figure 4.5 includes the microdosimetric spectra acquired at the same points. For the interval 7.85 mm – 8 mm, the changes in the spectra with a step of 50 μm are minor, as shown in figure 4.6 that for clarity's sake only its limits are included.

The summary of these sets of measurements complete the microdosimetric profile and the characterization of this irradiation field.

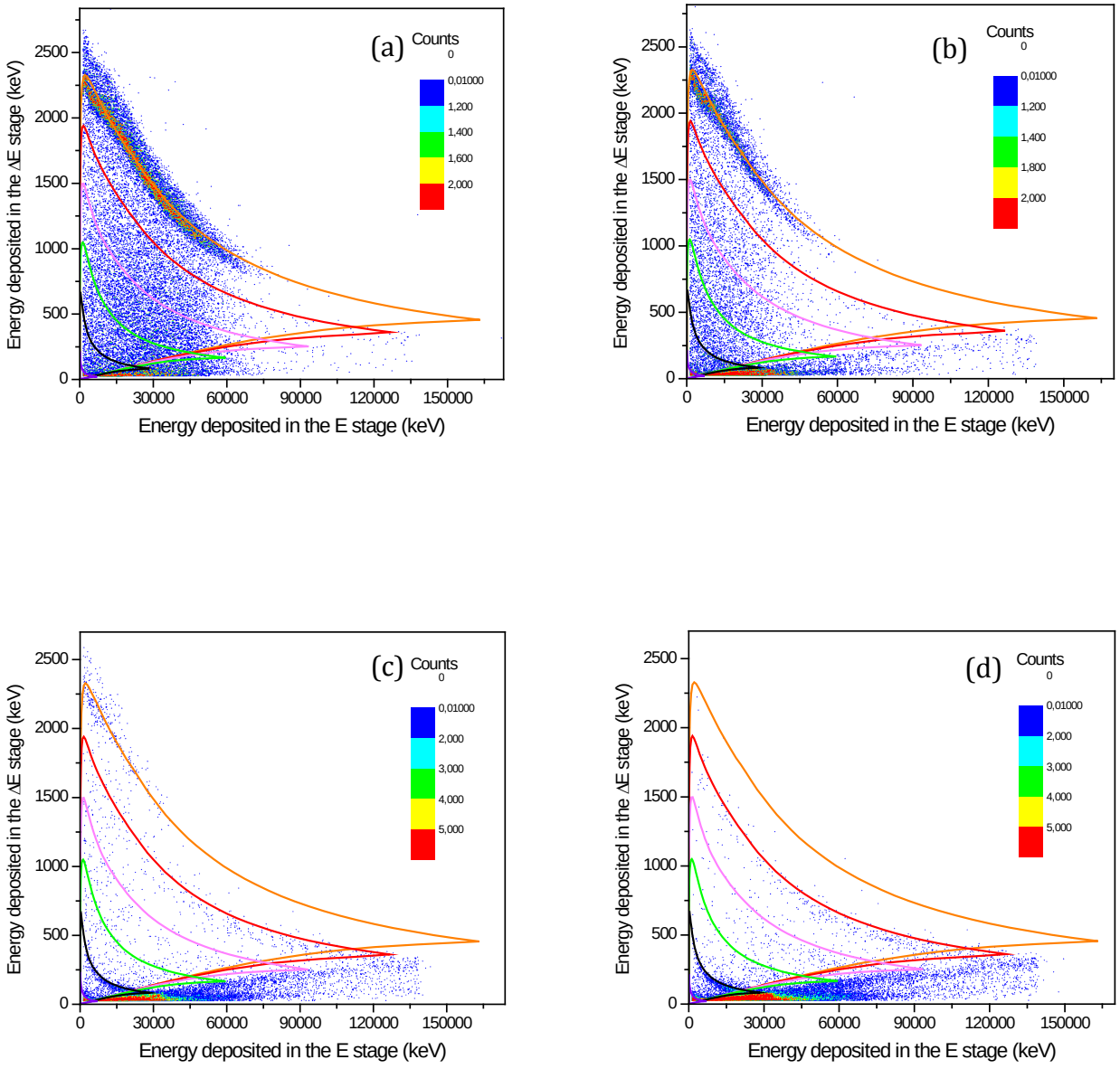

Figure 4.4: ΔE-E scatter plots measured across the fall off region of the Bragg peak, at the phantom depth of (a) 7.7 cm, (b) 7.75 cm, (c) 7.8 cm and (d) 7.85 cm.

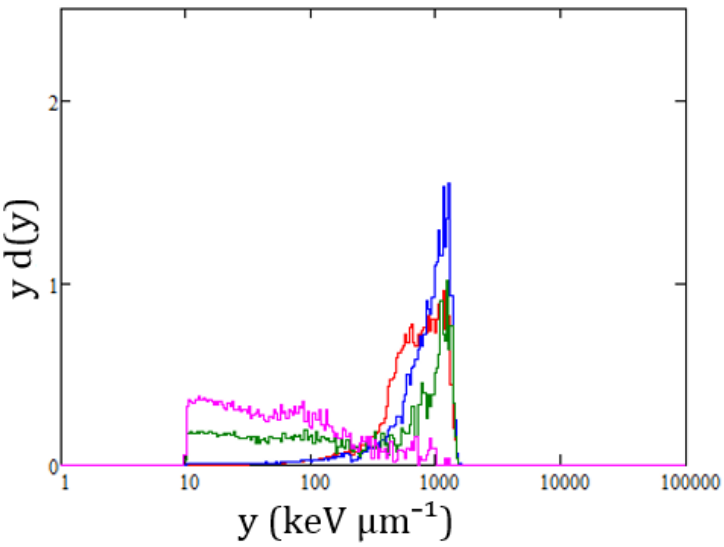

Figure 4.5: Lineal energy spectra obtained with the pixelated silicon microdosimeter at PMMA depths of 7.7 mm (red curve), 7.75 mm (blue curve), 7.8 mm (green curve) and 7.85 mm (pink curve), corrected adequately.

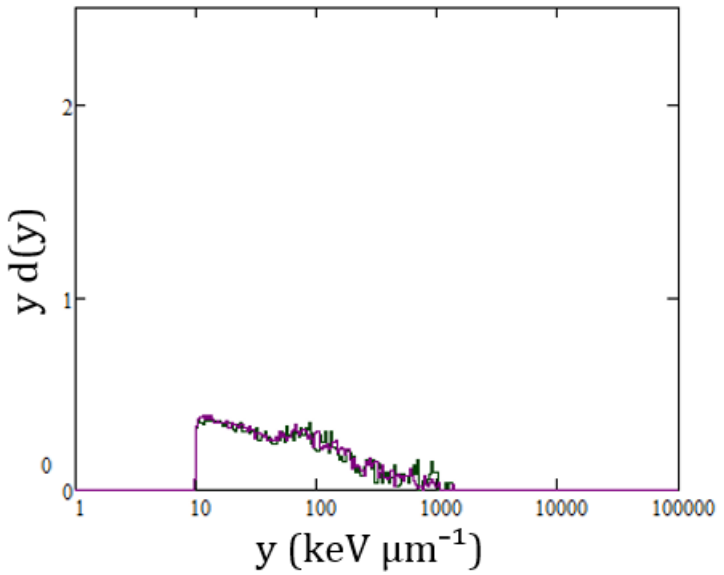

Figure 4.6: Lineal energy spectra obtained with the pixelated silicon microdosimeter at PMMA depths of 7.85 mm (green curve) and 8 mm (purple curve), corrected adequately.

CHAPTER 5

Characterization of a 290 AMeV carbon ion beam at the HIMAC facility

Past experimental experience, including preliminary measurements performed by irradiation a monolithic silicon telescope with a 62 AMeV carbon ion beam at the CATANA facility, encouraged to proceed to the study of higher energy therapeutic carbon ion fields.

This chapter includes the numerical and experimental study carried out to characterize a 290 AMeV carbon ion beam at the HIMAC facility. During the experimental campaign both monolithic and pixelated silicon detectors were irradiated with a carbon beam of 290 AMeV, pristine and Spread-Out Bragg peak. The detector was placed inside a PMMA phantom and microdosimetric spectra were acquired for various depths along the Bragg peak. A theoretical study was also carried out by performing Monte Carlo simulations (FLUKA code package) that reproduced the experimental conditions of the irradiations.

5.1 The HIMAC facility

The National Institute of Radiological Sciences (NIRS) is equipped with the Heavy Ion Medical Accelerator in Chiba (HIMAC) for cancer therapy with charged particles and its related basic studies. HIMAC is an accelerator complex that consists of a two-synchrotron ring system which is preceded by heavy-ion linacs and then is separated into a vertical and a horizontal beam transport lines [55].

Ion species ranging from He to Ar are accelerated to different energies varying from 100 AMeV to 800 AMeV. After its extraction from the synchrotron ring, the beam is delivered through the beam transport lines to six irradiation rooms that include three treatment rooms and the rooms for physics and general purpose experiments, secondary beam experiments and biological experiments. The capability of having different energies of both vertical and horizontal beams is essential for highly-controlled dose distribution and enables also the development of diagnostic applications. An overview of the entire facility's structure is shown on figure 5.1.

HIMAC has been functional since 1993, but the first clinical trial of heavy-ion radiotherapy started in June 1994 with 290 AMeV carbon ions for head and neck tumor patients. By June 2012, 6.512 patients had been treated in total using fully-stripped carbon ion beams of 290, 350, and 400 AMeV [56, 57].

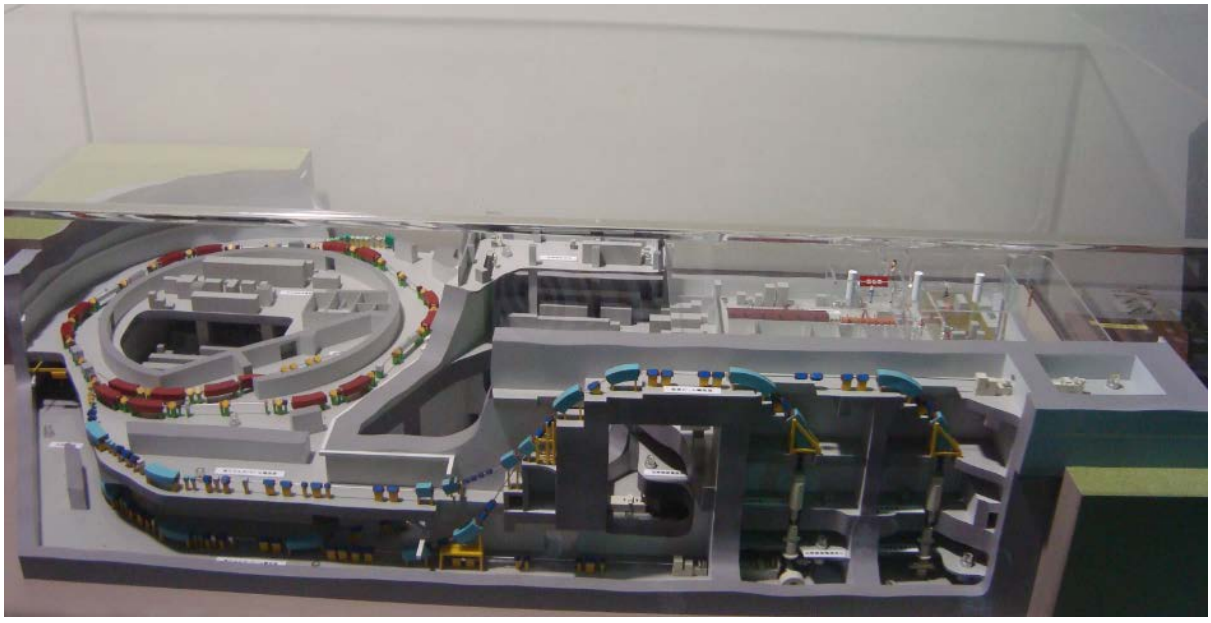

Figure 5.1: A 3D reconstruction of the accelerator facility structure.

5.2 The irradiation set-up

Two sample detectors with different ΔE stage design were selected to be irradiated with a 290AMeV carbon ion beam: the standard prototype (MST) and the ΔE stage segmented device (SMST). Measurements were performed with both pristine and Spread-Out Bragg peak for different points along the beam inside a PMMA phantom. PMMA blocks of different thicknesses were combined and placed in front of the detector in order to change the detector position across the Bragg peak. Figure 5.2 shows a picture of the experimental set-up.

Both detector stages were biased and the signals acquired were amplified and shaped by using two independent electronic chains.

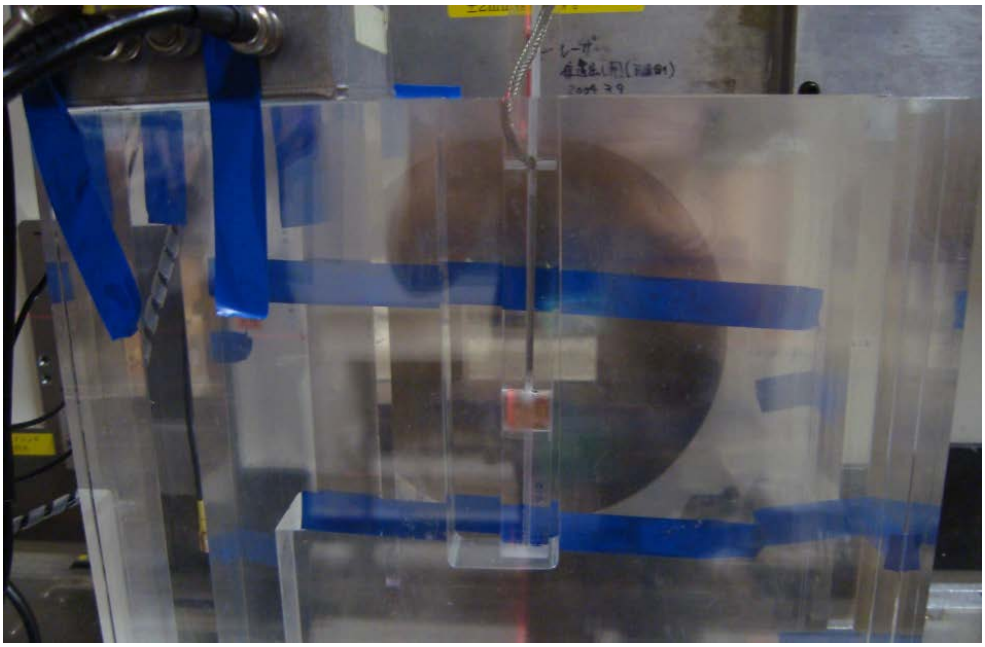

Figure 5.2: A picture of the irradiation set-up. The silicon device is placed at a fixed position and the thickness of the phantom is controlled by combining plates of different thickness. The alignment of the detector's sensitive area with the beam is done with a laser beam. On the top of the phantom the electronics boxes are placed.

A pair of wobbler magnets and a scatterer were used for the production of uniform irradiation fields. The Bragg peak was spread out in the depth-dose distribution of the heavy ions by a ridge filter. Figure 5.3 is a sketch of the experimental set-up including the beam delivery system.

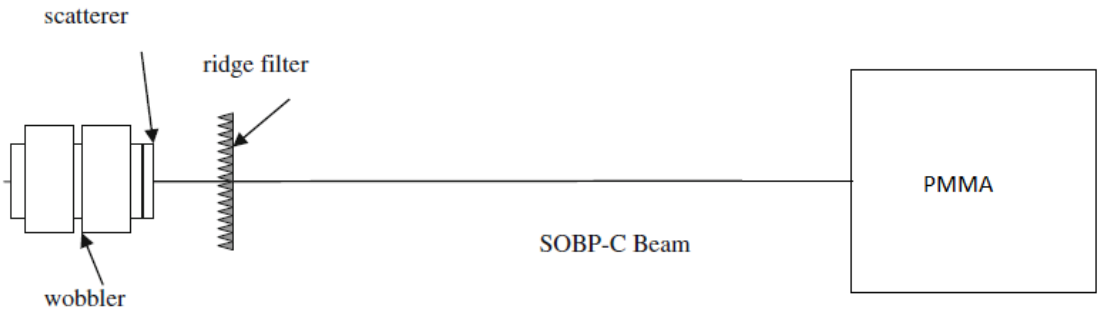

Figure 5.3: Sketch of the experimental set-up used to measure the microdosimetric spectra of the 290 AMeV SOBP carbon beam. The carbon beam was incident to the PMMA phantom and spectra were obtained placing the silicon microdosimeter at different depths inside the phantom.

A set of weighted monoenergetic beams shifted in depth is summed up to have uniform biological effect throughout the peak of the Spread-Out Bragg peak. Figure 5.4 (i) and (ii) show the physical depth dose distribution in water of the 290 AMeV pristine and therapeutic carbon ion beam, respectively.

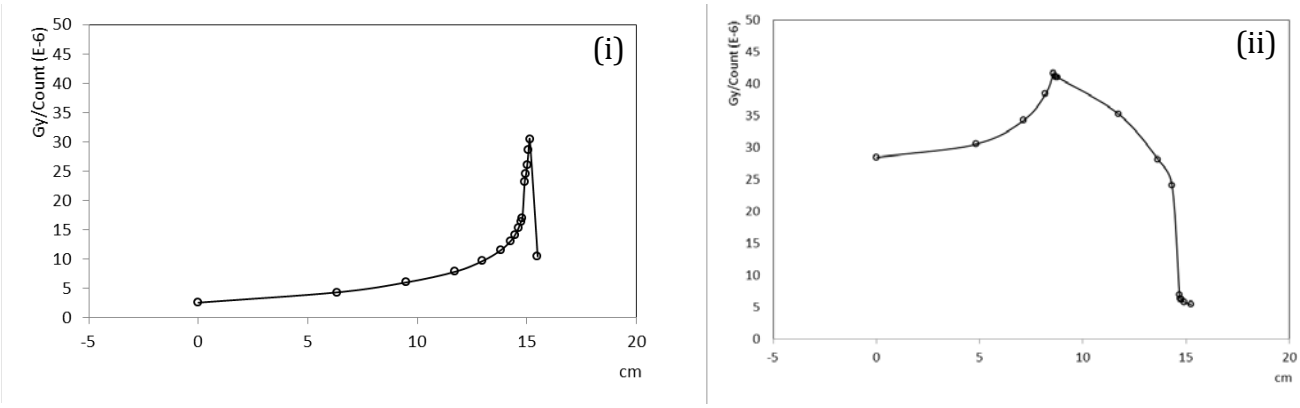

Figure 5.4: Physical depth dose distributions of a 290 AMeV pristine (i) and therapeutic carbon ion beam (ii), respectively.

5.3 Experimental results

The monolithic silicon microdosimeter and its segmented version were irradiated with a 290AMeV carbon ion beam. Measurements were performed with both pristine and Spread-Out Bragg peak for a significant amount of points across the beam inside a PMMA phantom. The points that were chosen are representative of the different parts of the Bragg peak: proximal part, Bragg peak and distal part. The interest was focused mainly on the Bragg peak and its distal part were the light ion fragments are detected and in order to observe the passage from one part to the other, the step of the measurements was set to 0.5 mm.

5.3.1 Irradiation of the monolithic silicon standard prototype (MST) with a clinical carbon ion beam

The scatter plots of the energy imparted per event in the ΔE stage versus that deposited in the E stage, at three representative depths for the different parts of the Spread-Out Bragg peak are shown in figures 5.5. Figure 5.5 (a) shows a measurement point that belongs to the proximal part of the Spread-Out Bragg peak (82 mm), where carbon ions cross the silicon device. Figure 5.5 (b) is located at the region of the Spread-Out Bragg peak (128.5 mm), where the carbon edge is visible, while figure 5.5 (c) includes the measurement point related to the distal part of the Spread-Out Bragg peak (130 mm), where primary carbon ions have completely stopped and lighter ions are formed due to beam fragmentation. The contribution of each type of fragment can be distinguished through the analytical distributions that are also depicted on the scatter plots: carbon (orange curve), boron (red curve), beryllium (pink curve), lithium (green curve), helium (black curve) and hydrogen (purple curve).

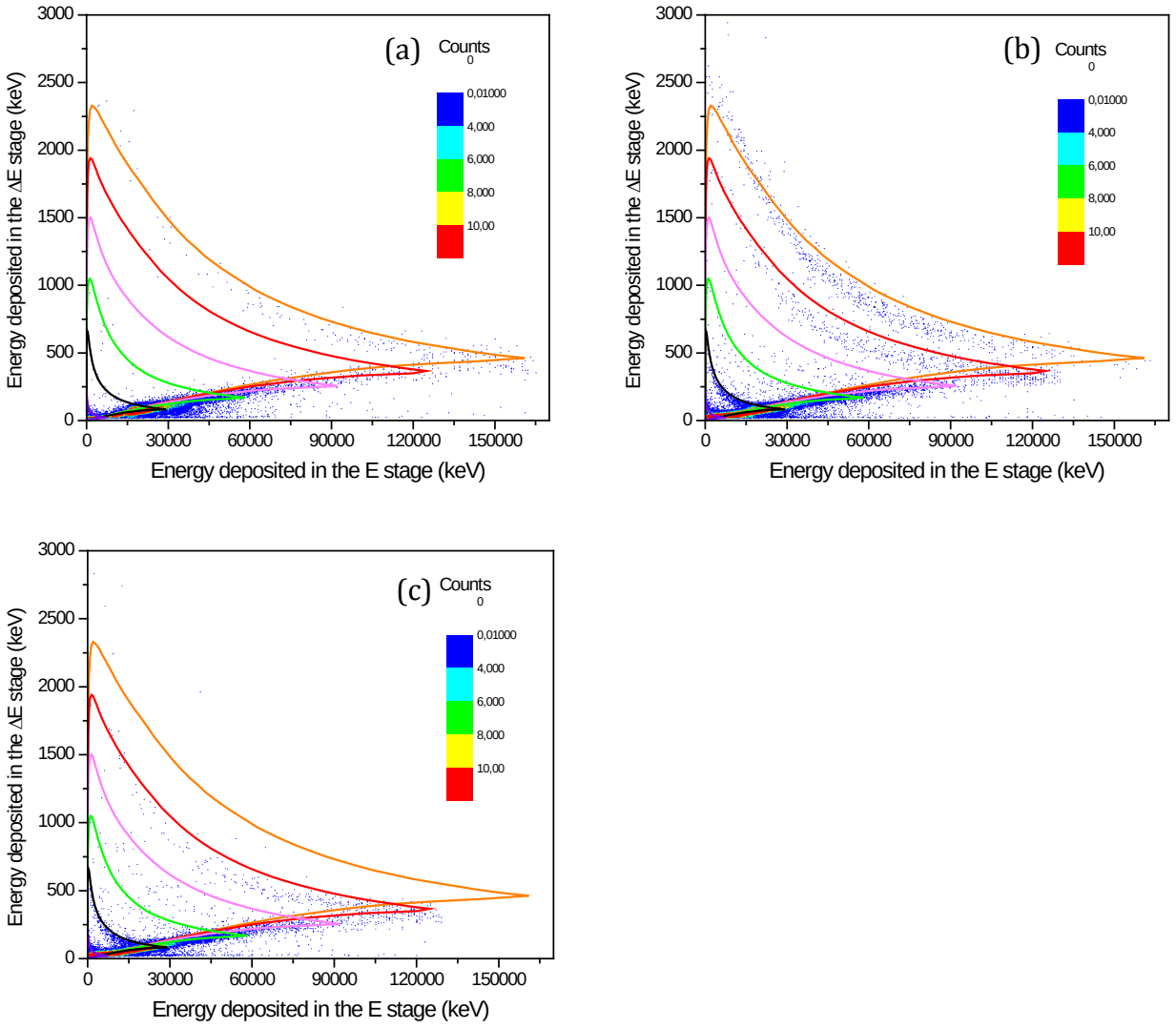

Figure 5.5: ΔE-E scatter plots measured with the MST at PMMA phantom depths (a) 82 mm, (b) 128.5 mm and (c) 130 mm, respectively.

The microdosimetric distributions after the necessary tissue-equivalence corrections for the same depths are shown in figure 5.6. The contribution to the lineal energy of each one of the fragments can be observed for the different measurement points. The increase of the population of events associated to light fragments (mainly hydrogen and helium) is clear at the low lineal energy values, by comparing the points 128.5 mm and 130 mm (blue and green curve, respectively), while the disappearance of the carbon ions is also obvious at the high lineal energy values for the same spectra comparison.

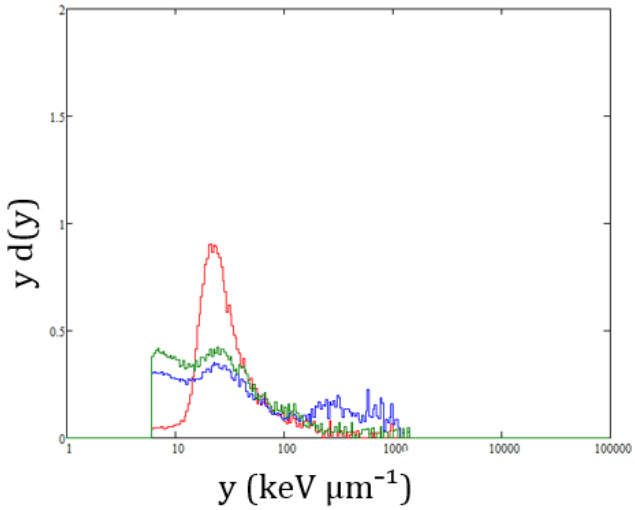

Figure 5.6: Lineal energy spectra acquired with the MST at PMMA phantom depths of 82 mm (red curve), 128.5 mm (blue curve) and 130 mm (green curve), corrected adequately.

5.3.2 Irradiation of the segmented ΔE stage silicon device (SMST) with a clinical carbon ion beam

The segmented ΔE stage silicon device was irradiated at several depths inside a PMMA phantom that correspond to different parts across and beyond the Spread-Out Bragg peak. The ΔE – E scatter plots that were acquired for two representative depths are shown in figures 5.7, together with the analytical distributions. The correspondence between type of ion and color of curve is kept the same as before (section 5.3.2). Figure 5.7 (a) is located at the region of the Spread-Out Bragg peak (128.5 mm), where the primary carbon beam together with the fragment formation can be observed, while figure 5.7 (b) shows the scatter plot acquired at the depth of 134 mm inside the PMMA phantom that corresponds to the region beyond the Bragg peak, where carbon ions are absent and beam fragments, mainly light ions are detected.

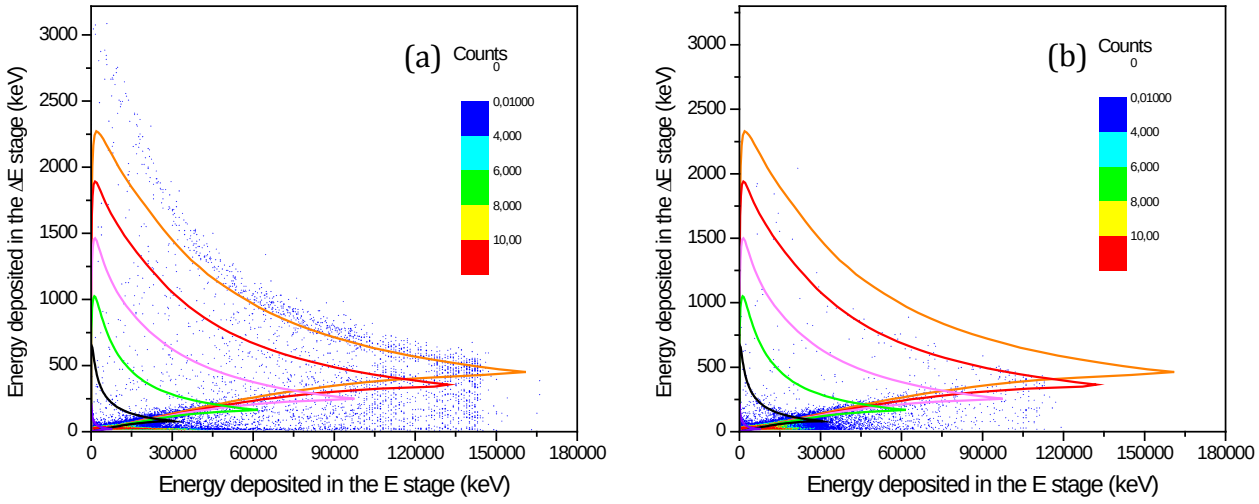

Figure 5.7: ΔE-E scatter plots measured with the SMST at PMMA phantom depths (a) 128.5 mm and (b) 134 mm, respectively.

The yd(y) distributions of the energy imparted in the ΔE stage corrected geometrically and for tissue equivalence for all the measurement points across the Spread-Out Bragg peak are shown in figures 5.8 (a) – (c). Figure 5.8 (a) includes the measurement points of the proximal part of the Spread-Out Bragg peak (70 mm, 82 mm and 115 mm). The lineal energy is progressively increasing as the measurement points are moving closer to the carbon edge. Figure 5.8 (b) shows the lineal energy distribution of two consecutive points across the Bragg peak with a difference of 50 μm (128 mm and 128.5 mm) and (c) includes points corresponding to the distal part of the Bragg peak (130 mm and 134 mm). Even with such a small step as 50 μm, the difference in the contribution of the primary carbon ion beam to the high lineal energy values is noticeable, as shown in figure 5.8 (b). On the contrary, for the distal part of the Bragg peak, a "saturation" point in the fragment production seems to be reached, thus no difference can be observed despite the step of 4 mm between the measurement points. Figure 5.8 (d) summarizes

the lineal energy distribution of all the previous points, excluding for clarity's sake two points (128 mm and 130 mm) that their pair measurements as presented in figures 5.8 (b) and (c) are very similar.

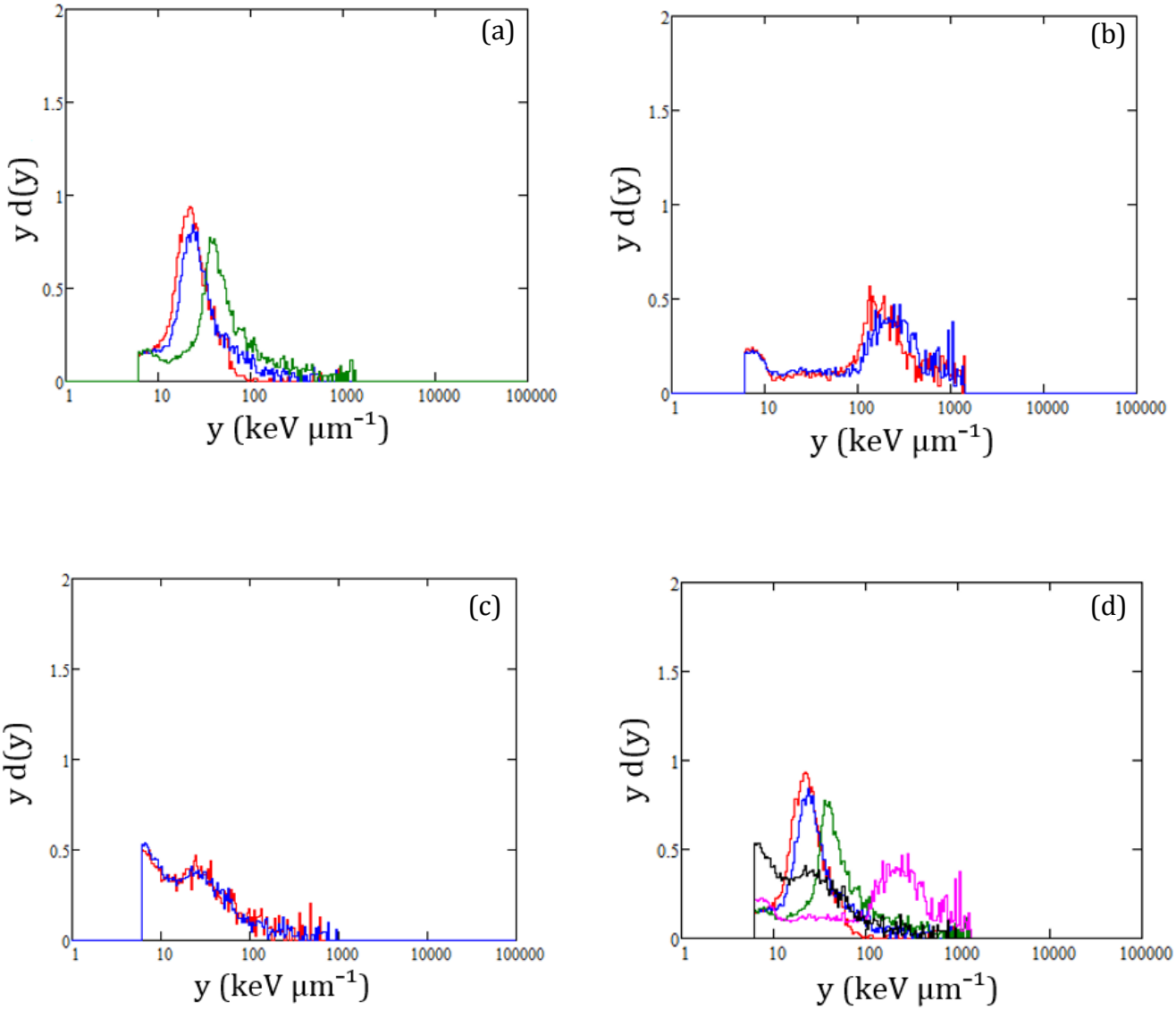

Figure 5.8: Lineal energy spectra acquired with the SMST at several PMMA phantom depths: (a) 70 mm (red curve), 82 mm (blue curve) and 115 mm (green curve), (b) 128 mm (red curve) and 128.5 (blue curve), (c) 130 mm (red curve) and 134 mm (blue curve) and (d) 70 mm (red curve), 82 mm (blue curve), 115 mm (green curve), 128.5 (pink curve) and 134 mm (black curve).

5.3.3 Irradiation of the monolithic silicon standard prototype (MST) with a pristine carbon ion beam

The scatter plots of the energy ε imparted to the ΔE and the E stage at each depth are shown in figures 5.9. The plots are scaled accordingly to fully depict the statistics. Figure 5.9 (a) shows a measurement point that belongs to the proximal part of the Bragg peak (58 mm), where carbon ions cross the silicon device and mainly protons (purple curve) and alpha particles (black curve) can be observed. Figure 5.9 (b) is located at the region of the Bragg peak (127 mm), where the carbon edge is visible (analytical distribution represented by the orange curve), while figures 5.9 (c) and (d) include measurement points related to the distal part of the Bragg peak (128.5 mm and 131 mm, respectively), where primary carbon ions have completely stopped and lighter ions are formed due to beam fragmentation.

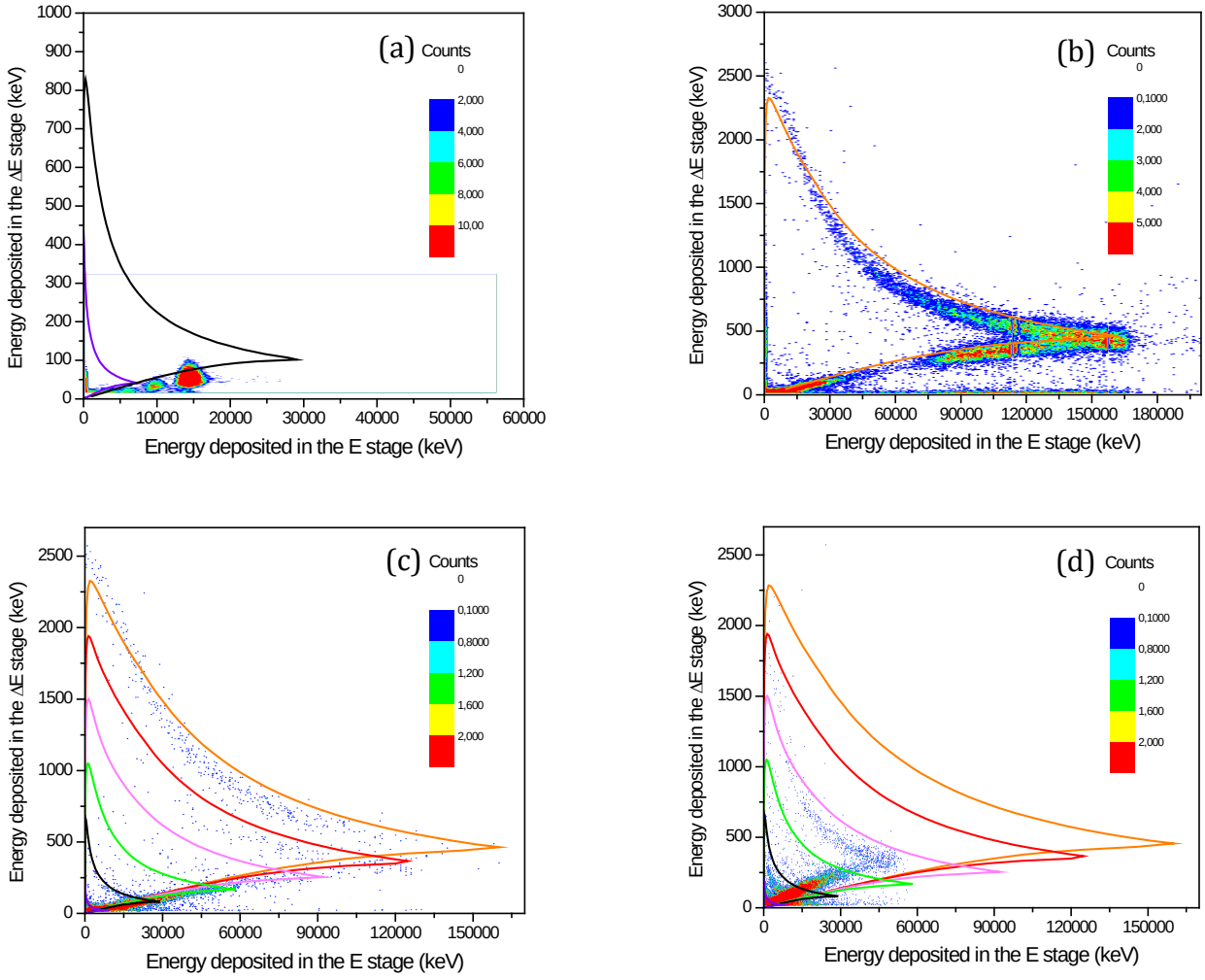

Figure 5.9: ΔE-E scatter plots measured with the MST at PMMA phantom depths (a) 58mm, (b) 127mm, (c) 128.5 mm and (d) 131 mm, respectively.

The microdosimetric lineal energy spectra obtained with the MST device at several phantom depths, after the adequate corrections are shown in figures 5.10 (a)-(c). Figure 5.10 (a) includes the spectra acquired at measurement points at the proximal part of the Bragg peak and figure 5.10 (b) at the distal part of the Bragg peak. Figure 5.10 (c) shows the rest of the measurement points at the distal part of the Bragg peak that were omitted for clarity's sake. After the depth of 129 mm, no significant change in the lineal energy distributions are observed.

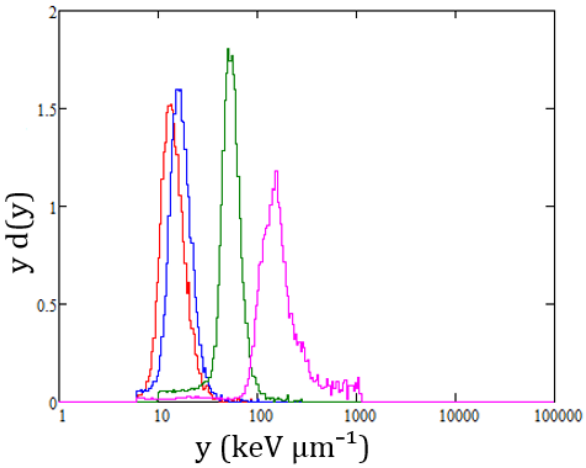

Figure 5.10 (a): Lineal energy spectra acquired with the MST at PMMA phantom depths of 10 mm (red curve), 58 mm (blue curve), 106 mm (green curve) and 127 mm (pink curve), corrected adequately.

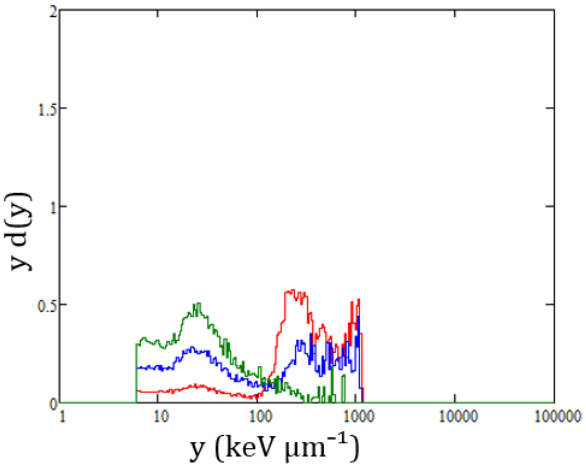

Figure 5.10 (b): Lineal energy spectra acquired with the MST at PMMA phantom depths of 128 mm (red curve), 128.5 mm (blue curve) and 129 mm (green curve), corrected adequately.

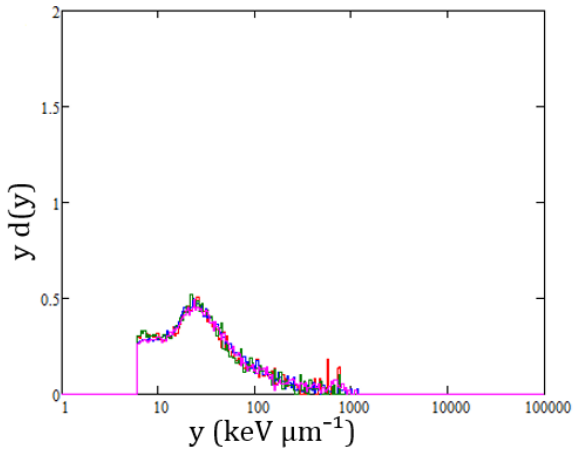

Figure 5.10 (c): Lineal energy spectra acquired with the MST at PMMA phantom depths of 129 mm (red curve), 129.5 mm (blue curve), 130 mm (green curve) and 131 mm (pink curve), corrected adequately.

5.3.4 Revision of the experimental results

a) Comparison between pristine and Spread-Out Bragg peak carbon ion beam

The microdosimetric spectra acquired with the MST device in monoenergetic and clinical carbon ion field at the same phantom depths were compared. Figures 5.11 (a) and (b) show the spectra acquired with pristine (green curve) and Spread-Out Bragg peak (purple) carbon ion beam at the phantom depth of (a) 128.5 mm and (b) 130 mm.

Both spectra are similar for the different irradiation fields. Figure 5.11 (a) shows higher low y values for the clinical field, a phenomenon that is reversed for high y values. The excess of the low y values in the clinical field in comparison to the monoenergetic is present also in figure 5.11 (b), but in this case of high y values for both fields are in agreement. This behavior can be attributed to the summation of the fragmentation tail of more proximal peaks. This statement could be enhanced with a comparison for points in shallower depths, since both points compared belong to the distal part of the Bragg peak, but unluckily data were not available.

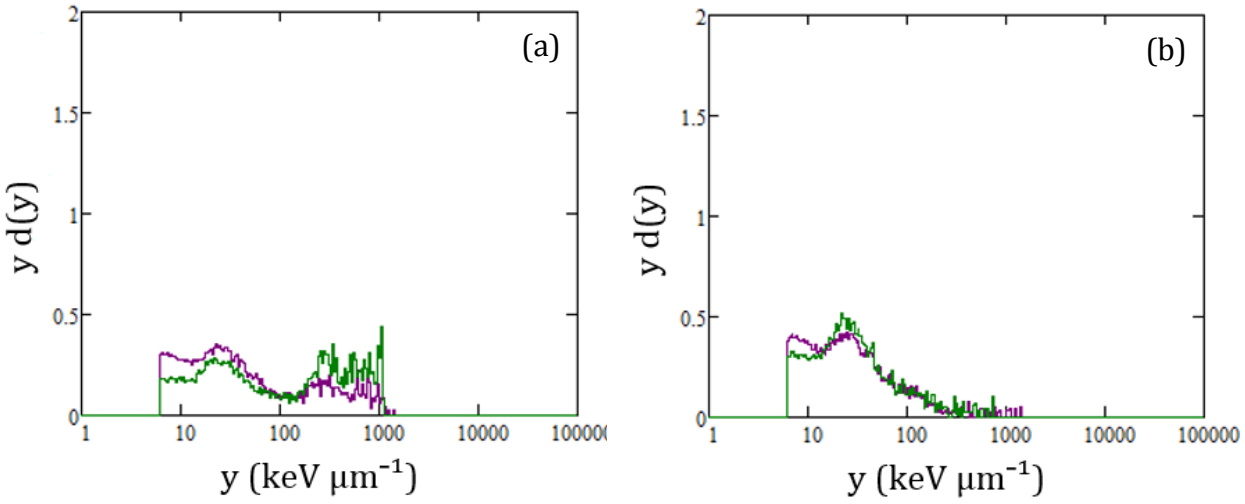

Figure 5.11: Lineal energy spectra acquired with the MST in monoenergetic (green curve) and clinical (purple curve) carbon ion field at PMMA phantom depth (a) 128.5 mm and (b) 130 mm, respectively.

b) Comparison between MST and SMST

Based to the experimental data that were available, the comparison between the MST and SMST devices was possible for three measurement points: (a) 82 mm, (b) 128.5 mm and (c) 130 mm (figures 5.12). Each of the measurement points compared represent a different part of the sprectrum: (a) proximal part, (b) Bragg peak and (c) distal part of the Spread-Out Bragg peak. Figures 5.12 show a good agreement of the spectra compared for all of the measurement

points along the Spread-Out Bragg peak. The discrepancy at low y-values that is present in figures 5.12 (a) and (c) is due to the geometrical differences of the sensitive volumes of the ΔE stage. Despite this discrepancy, the agreement between the two devices is satisfactory.

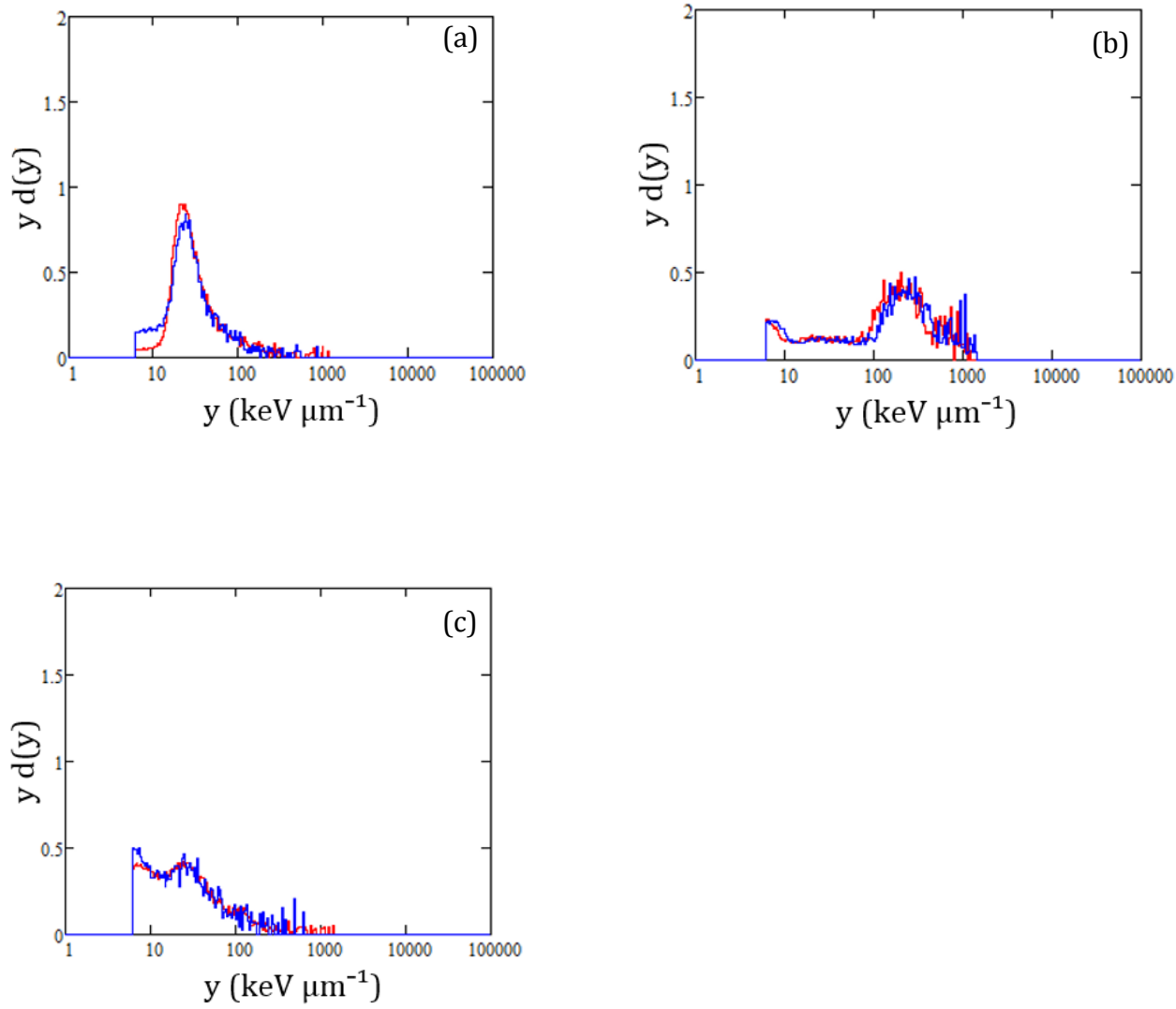

Figure 5.12: Lineal energy spectra acquired with the MST (red curve) and the SMST (blue curve) in clinical carbon ion field at PMMA phantom depth (a) 82 mm, (b) 128.5 mm and (c) 130 mm, respectively.

5.4 Experimental results and comparison with FLUKA simulations

For case of the irradiation of the monolithic silicon standard prototype with a pristine beam, Monte Carlo simulations were performed for some representative points along the Bragg peak, by using the FLUKA simulation package [58, 59].

The geometry used in the simulations reproduces the one that was used in the irradiations. A parallelepiped PMMA phantom was irradiated with an expanded, aligned and unmodulated beam of 290 AMeV (figure 5.13). The dimensions of the detector were simulated were 1.9 μm in thickness for the ΔE and 500 μm in thickness for the E stage. The plastic rod that contained and supported the detector (figure 5.2) was simulated with a density of 1.19 g/cm^3 that differs from the one of the PMMA phantom (1.31 g/cm^3).

Microdosimetric spectra were scored in the telescope detector by considering single events of energy deposition inside the ΔE and the residual energy stage. The monolithic detector was placed at some of the representative phantom depths of the measurement campaign. Scatter plots of energy deposited in the ΔE stage against that deposited in the E stage were assessed, thus allowing the contribution of carbon ion fragments to the calculated microdosimetric spectra to be studied.

For saving computational time, the phantom was divided in two regions: 1) a "high precision" region upstream of the detector, inside the detector and 2) the region downstream of the detector. The details about the input options for particle transport setting are discussed in the following.

The step length for multiple Coulomb scattering of charged hadrons was set in order to give the 1% of the maximum energy loss in each step (FLUKAFIX input option in the FLUKA code) for all materials considered in the simulations. For electrons the step of multiple Coulomb (EMFFIX input option in the FLUKA code) scattering was set at 5%. A higher value was set in the phantom region downstream of the detector, in order to save computing time.

The cut-off energy for delta-ray production (DELTARAY input option in the FLUKA code) was set at 100 keV in all the simulated materials other than the region downstream of the detector which was assigned 1 MeV, again to save computing time. The energy transferred below this cut-off is treated under the continuous energy-loss assumption, while delta-ray electrons are transported above. Particle transport was not switched off in the downstream region for simulating, although in an approximate way, their contribution to electron equilibrium in the detector.

Restricted energy-loss fluctuations (i.e. energy straggling) were switched on for charged hadrons and electrons in all the simulated materials (IONFLUCT input option in the FLUKA code). The accuracy of energy-loss fluctuations was set to the minimum allowed value in FLUKA in the region downstream of the detector for saving the computing time.

The energy cut-off for particle transport was set to 1 keV for carbon ions, electron and photons in all regions except for that downstream of the detector (electron and photon cut-off 5 MeV).

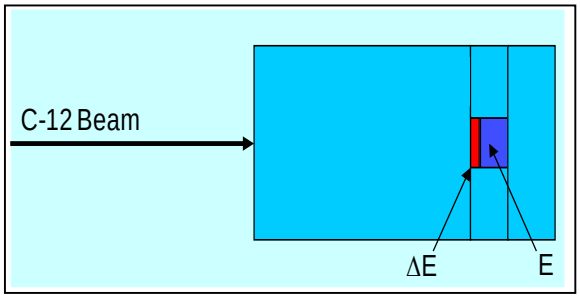

Figure 5.13: A schematic view of the simulated geometry that reproduces the one used in the irradiations at the HIMAC facility.

Figures 5.14 (a) – (d) show the comparison between the measured distributions of the energy imparted in the E stage (blue curves) and the ones simulated with the FLUKA code package (red curves). The energy distributions include geometrical and tissue corrections.

In the simulated distributions the energy is deposited about 1 mm shallower in thickness inside the phantom in comparison to the measurements. Figures 5.15 (a) and (b) show the agreement between a simulated microdosimetric spectrum at a certain phantom depth and a measured spectrum acquired 1 mm further than the simulated depth.

Since the uncertainty associated to each measurement position was about 1 mm and this behavior is consistent for all the positions compared, the discrepancy is considered to be acceptable.

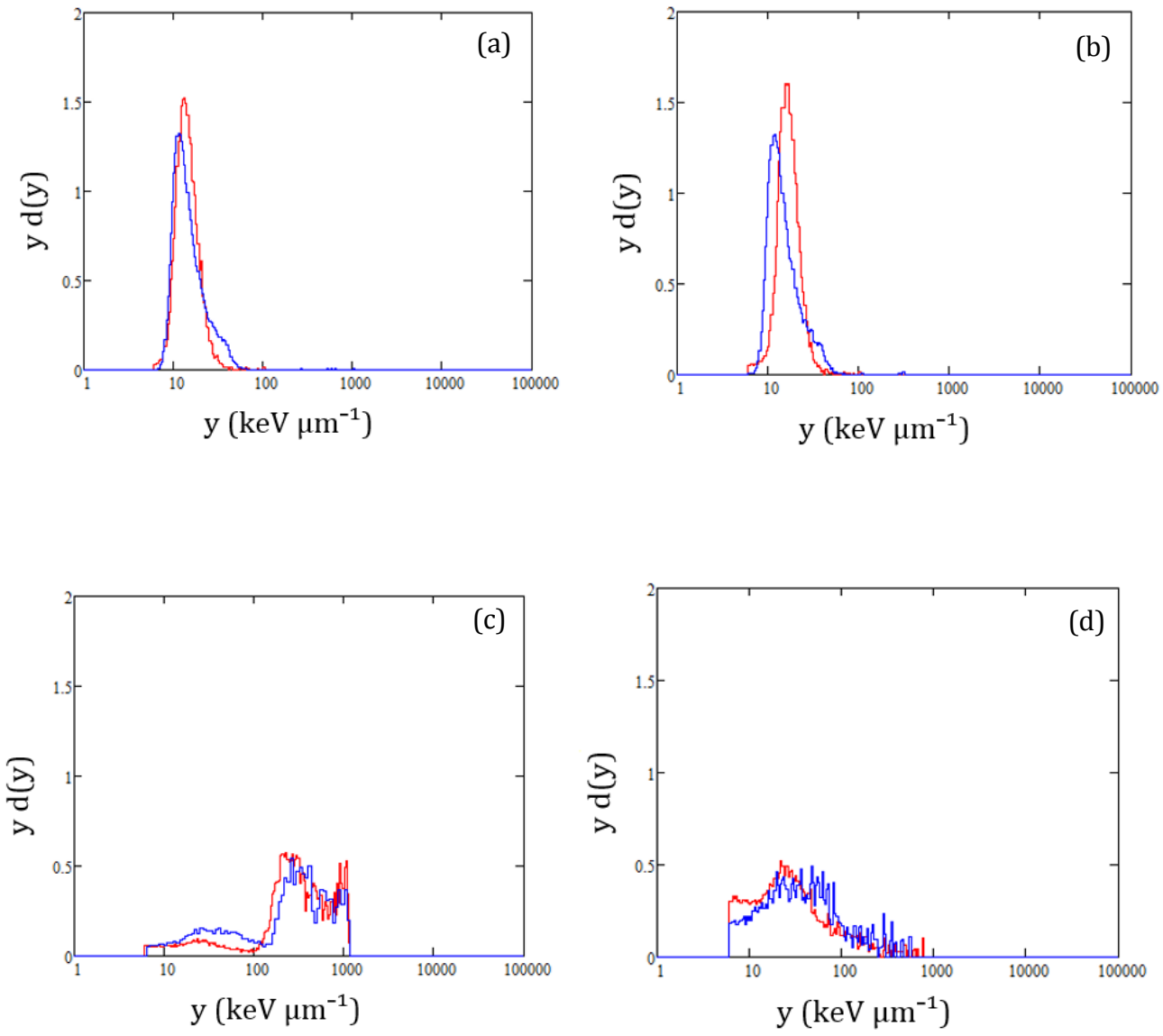

Figure 5.14: Comparison between the microdosimetric spectra acquired with the MST corrected adequately geometrically and for tissue equivalence (red curve) and those simulated with the FLUKA code package (blue curve). The measurement points shown on the figures are: (a) 10 mm, (b) 58 mm, (c) 128 mm and (d) 130 mm, respectively.

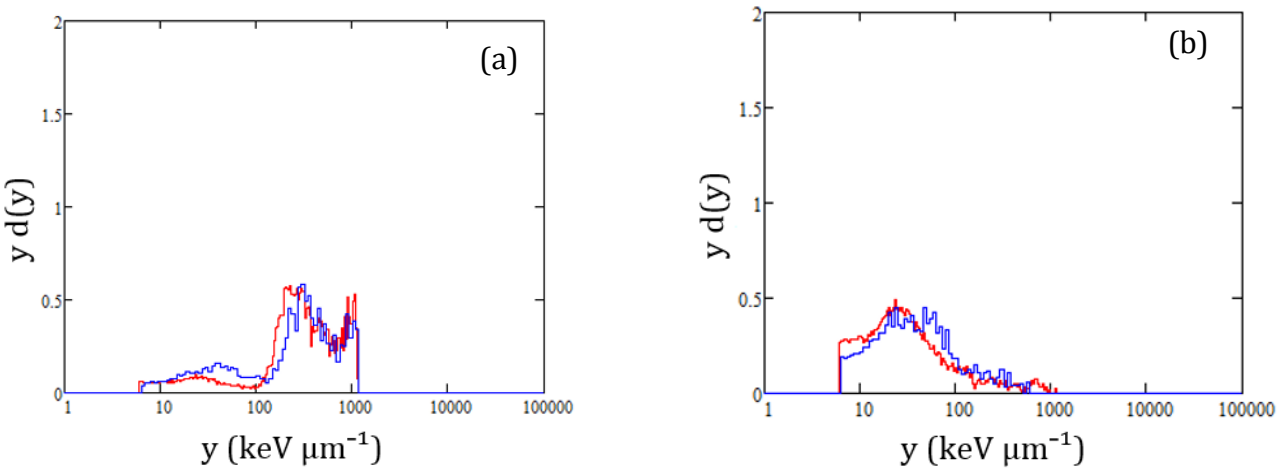

Figure 5.15: Comparison between the microdosimetric spectra acquired with the MST corrected adequately geometrically and for tissue equivalence (red curve) and those simulated with the FLUKA code package (blue curve). The measurement points shown on the figures are: (a) 128 mm measured (red curve) and 127 mm simulated (blue curve) and (b) 131 mm measured (red curve) and 130 mm simulated (blue curve).

CHAPTER 6

Preliminary measurements with a 362 AMeV clinical carbon ion beam at the CNAO facility

The achievement of reproducibility during the measurement campaign at the CATANA facility and the successful characterization of two carbon ion fields of 290 AMeV at the HIMAC facility enhance the confidence on the detectors' performance in high energy carbon ion fields and motivate to aim in seek of their limitations, by increasing the energy of the irradiation and testing different irradiation conditions.

The preliminary measurements at the CNAO facility were performed from this perspective, by irradiating a segmented silicon microdosimeter with a 362 AMeV carbon ion clinical Spread - Out Bragg Peak inside a water phantom. Microdosimetric spectra were obtained at the same points also with a mini-TEPC, enabling the direct comparison of the results and provided an experimental confirmation of the silicon microdosimeter effectiveness.

6.1 The CNAO facility

The "Centro Nazionale di Adroterapia Oncologica" (CNAO) is the National Centre for Oncological Hadrontherapy and the first hospital in Italy specifically dedicated to tumor treatment by using proton and carbon ion beams, where about 500 patients have been treated since September 2011. Heretofore 23 clinical protocols have been used to treat various types of gliomas and sarcomas, while clinical trials are foreseen for diseases such as Hodgkin Lymphoma, lung cancers, melanoma of rectum and vagina and pediatric tumors [60].

The accelerator complex is based on a 25 m diameter and 80 m long synchrotron capable of accelerating carbon ions up to 400AMeV and protons up to 250MeV that are extracted to one of the three treatment rooms and active scanning is used as a beam delivery system [61]. The scanning system includes two identical dipole magnets for horizontal and vertical beam deflection, each one connected to a fast power supply. The dose delivery system exploits a set of monitor chambers to measure the fluence and position of the beam and drives the beam during the treatment by controlling the sequence of currents set by the power supplies [62]. Figure 6.1 shows a picture of a part of the synchrotron acceleration ring.

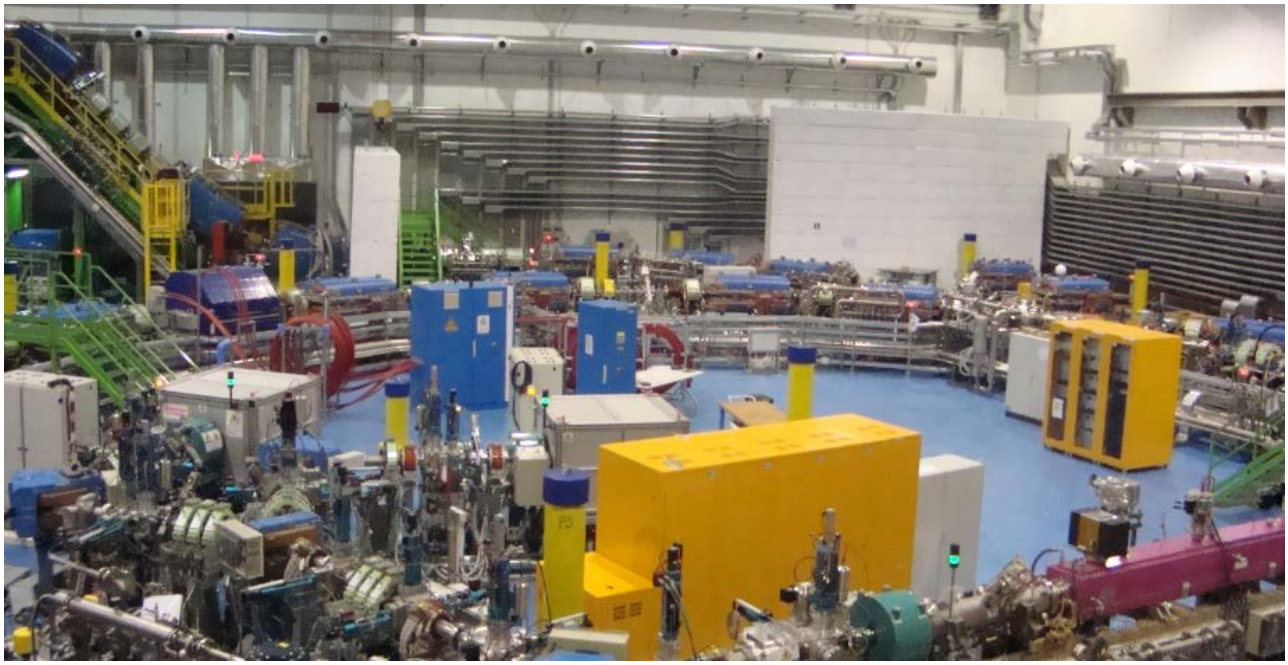

Figure 6.1: A picture of the synchrotron acceleration ring at the CNAO facility.

6.2 The irradiation set-up

The measurements were carried out with the pixelated silicon microdosimeter (SMST) inserted in a plastic tube at different depths inside a cubic water phantom along the Spread-Out Bragg peak. The beam was composed of 18 energies between 328 AMeV and 362 AMeV, spread at about 3 cm and during each irradiation 1 Gy was delivered at the isocenter of a 30x30x30 mm^{-3} water phantom. The beam energy components with their adequate weights are shown analytically in table 6.1.

# slice	Energy (MeV/u)	Weight
1	328.1	0.01083107
2	330.2	0.02375417
3	332.2	0.02882543
4	334.1	0.02856271
5	336.1	0.03081029
6	338.1	0.03054569
7	340.1	0.03401608
8	342.1	0.03603699
9	344.0	0.03438200
10	346.0	0.05978265
11	348.0	0.03673941
12	349.9	0.04458568
13	351.9	0.04950121
14	353.8	0.05683604
15	355.7	0.06194062
16	357.7	0.08632996
17	359.6	0.08724053
18	361.5	0.25927945

Table 6.1: The analytical composition of the Spread-Out Bragg peak by 18 energies between 328 AMeV and 362 AMeV with their adequate weight.

Figure 6.2 shows the experimental set-up used during the irradiations. As a measurement position the distance between the external phantom surface and the detector surface was considered.

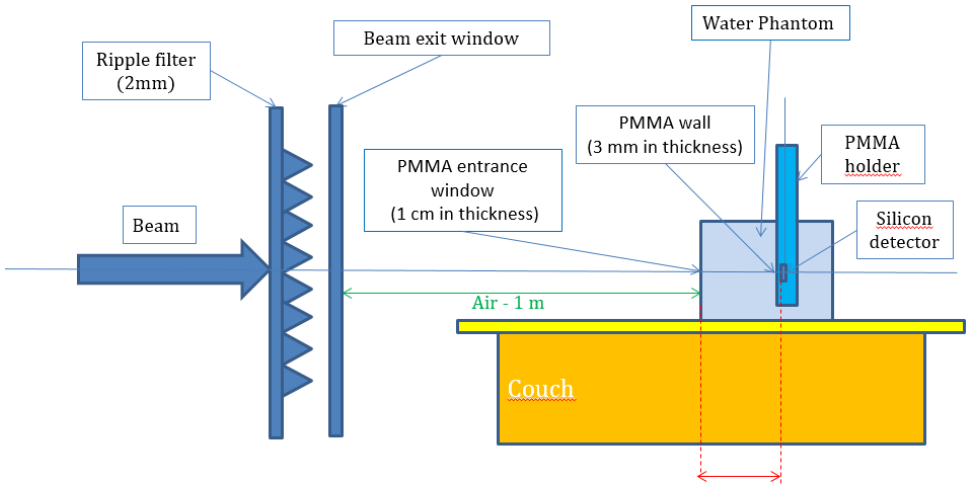

Figure 6.2: A sketch of the experimental set-up used to measure the microdosimetric spectra of the 362 AMeV SOBP carbon beam. The carbon beam was incident to the water phantom and spectra were obtained placing the silicon microdosimeter at different depths inside the phantom.

Microdosimetric spectra were obtained at the same measurement points also with a mini-TEPC, filled with tissue equivalent propane at the pressure of 622 mbar corresponding to 1 µm of tissue and was biased at 600 V. The measurements with the silicon microdosimeter were carried out first for all the different points followed by the measurements with the mini-TEPC. Figures 6.3 (a) and (b) show the set-up of the two detectors.

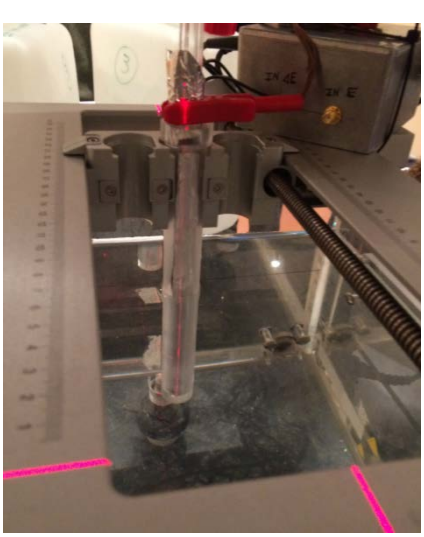

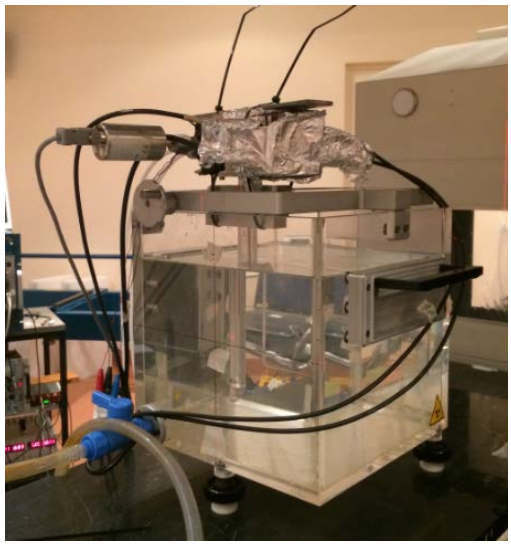

Figure 6.3: Pictures of the set-up of (a) the silicon microdosimeter and (b) the mini-TEPC.

6.3 Experimental results

During the experimental campaign consisting of three different shifts, measurements were carried out at different positions along the Spread-Out Bragg peak, inside the water phantom. The first shift was intended to set up the beam intensity parameters minimizing pulse pile up and optimizing the electronic signal acquisition. Measurements were carried out with increasing the beam density from 10^5 particles per spill to 10^8 particles per spill with degrader F50 and F20.

Due to the time consuming nature of the measurements because of the low dose delivered per irradiation, in combination with the limited availability of beam time, microdosimetric spectra with significant statistics were acquired for only two points across the Spread-Out Bragg peak: 205 mm and 215 mm. Figure 6.4 shows the lineal energy distributions acquired for these points with the silicon microdosimeter, corrected for geometrical and tissue equivalence.

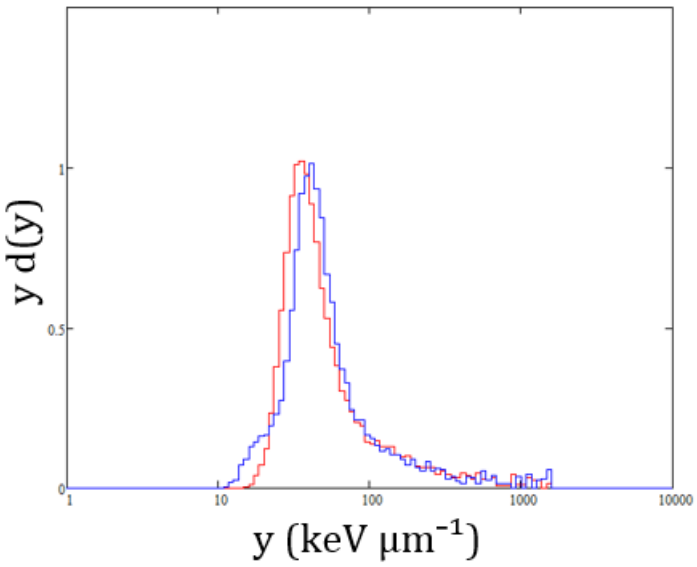

Figure 6.4: Lineal energy spectra acquired with the SMST at water phantom depths of 205 mm (red curve) and 215 mm (blue curve), corrected adequately.

Figures 6.5 (a) and (b) compare the microdosimetric spectra measured by the silicon telescope and the mini-TEPC at a depth of 205 mm and 215 mm, respectively, inside the water phantom irradiated with a clinical Spread-Out Bragg peak of maximum energy 362 AMeV carbon ions.

The agreement of the compared results is considered to be satisfactory. Minor deviations that occur can be due to uncertainty in the precision of positioning of the two detectors (their dimensions are of different order of magnitude with the silicon detector being in µm while mini-TEPC in mm) and to the uncertainties in the corrections of the microdosimetric spectra acquired with the silicon telescope for shape and tissue equivalence. Another factor that can

explain the difference in the compared spectra is the probable variation of the delivered field, since the measurements with the two different detectors were not performed at the same time but sequentially. The measurements with the silicon microdosimeters took place first for all the different points followed by the measurements with the mini TEPC, as already mentioned. The delivered fields were supposed to be identical for every one of the irradiations. However, while measurements were ongoing it was noticed that the hypothetically identical fields were not delivered in consistent time duration and this might have an impact in the quality of the delivered field.

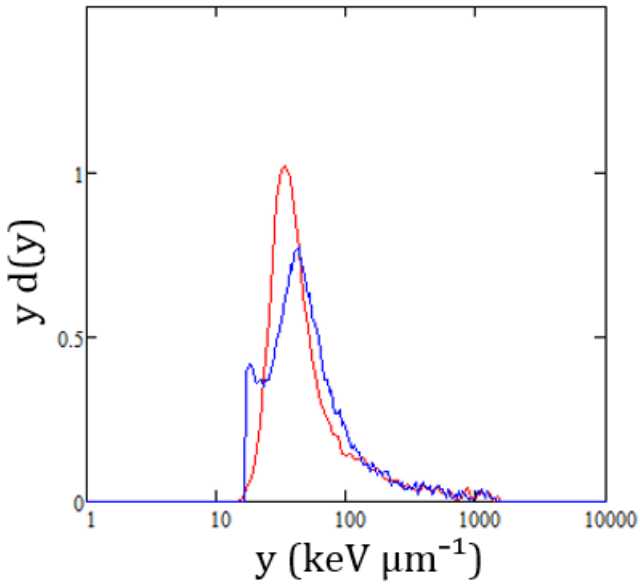

Figure 6.5 (a): Comparison between microdosimetric spectra measured by the silicon telescope (red curve) and the mini-TEPC at a depth of 205 mm inside a cubic water phantom irradiated with a clinical Spread-Out Bragg peak of maximum energy 362 AMeV carbon ions.

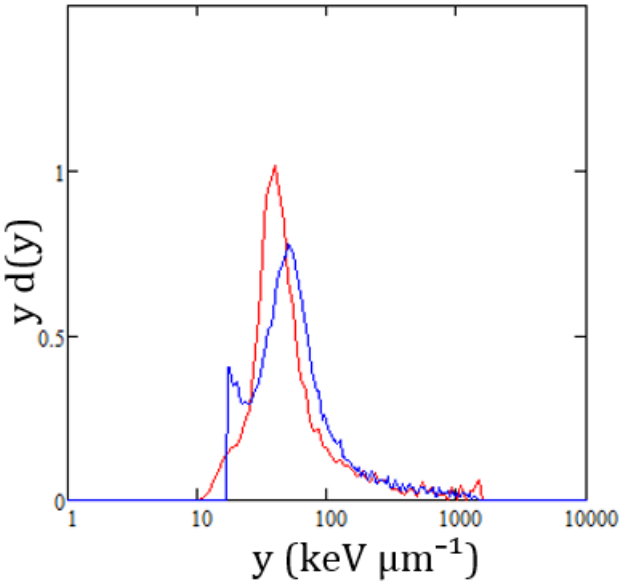

Figure 6.5 (b): Comparison between microdosimetric spectra measured by the silicon telescope (red curve) and the mini-TEPC at a depth of 215 mm inside a cubic water phantom irradiated with a clinical Spread-Out Bragg peak of maximum energy 362 AMeV carbon ions.

6.4 Preliminary numerical study with the FLUKA Monte Carlo code

A proposal to overcome the problem of long measurements and low statistics due to the low dose delivered per irradiation cycle is the measurement performance with monoenergetic fields. For this purpose, the response of a silicon telescope microdosimeter against 400 AMeV was calculated with Monte Carlo simulations by using the FLUKA code.

6.4.1 Simulation features

The geometry and the techniques that were used to save computational time are similar to the ones described in details in section 5.4. A parallelepiped PMMA phantom (density of 1.19 g/cm^3) was irradiated with an expanded, aligned and unmodulated beam of 400 AMeV carbon ion beam. The simulated beam cross section was 10×10 mm^2, the same of the FWHM transverse size of the one delivered in the CNAO treatment rooms. It should be stressed that active beam delivery system is used at CNAO for distributing the dose to the patient. The detector (10×10 mm^2 in active surface) was centered on the beam axis and was placed at various phantom depths.

6.4.2 Simulation results

This preliminary set of simulations aimed at calculating the depth dose distribution of primary carbon ions and secondary particles (generated mainly from carbon fragmentation) at various depths across the phantom. Subsequently, microdosimetric spectra were scored in the telescope detector by considering single events of energy deposition inside the ΔE and the residual energy stage. The energy deposited in the ΔE and E stages was scored event-by-event in order to preserve the correlation between the responses of the two elements, thus allowing to discriminate the contribution of carbon ion fragments to the calculated microdosimetric spectra.

The simulated depths across the Bragg peak were 1 cm, 10 cm (proximal to the Bragg peak), 23.5 cm (Bragg peak) and 26 cm (tail of Bragg peak) as shown in figure 6.6. It should be stressed that the depth-dose across the PMMA phantom was scored in regions 1×1 cm^2 wide. This allowed to obtain a sufficient statistics for fragment energy deposition in the tail at depths below the distal part of the Bragg peak. The simulations for calculating the detector response refer to energy deposition in regions 1×1 mm^2 wide, thus decreasing the scoring efficiency of a factor of about 100.

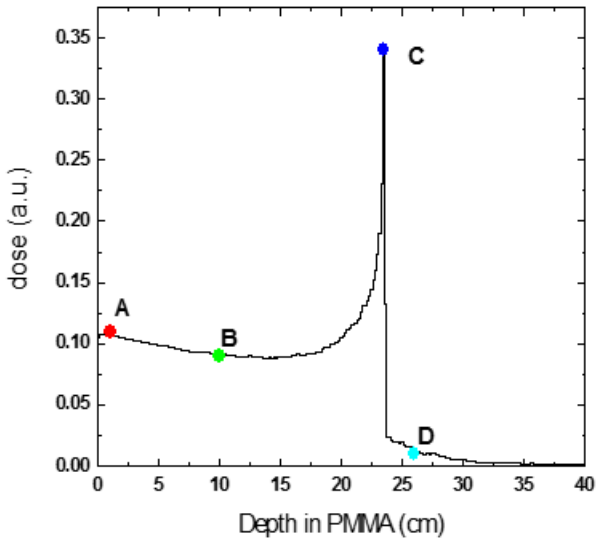

Figure 6.6: Depth dose profile of the 400 AMeV unmodulated carbon ion beam. The points A-D are the simulated depths (1, 10, 23.5 and 26 cm, respectively).

The scatter plots of the energy imparted per event in the ΔE stage versus that deposited in the E stage, at some simulated positions across the Bragg peak are shown in figures 6.7 (a) – (d). Different energy depositions in the two stages allow to distinguish the contribution of the primary beam (C) and of the fragments (B, Be, Li, He, H), as shown in figure 6.7 (b). The tail below the distal part of the Bragg peak is due to energy deposition from carbon ion fragmentation. The scatter plot simulated across this tail as shown in figure 6.7 (d) includes events mainly due to protons from fragmentation and elastic scattering from secondary neutrons. Heavier ions cannot be observed because of the insufficient statistics of the simulated data.

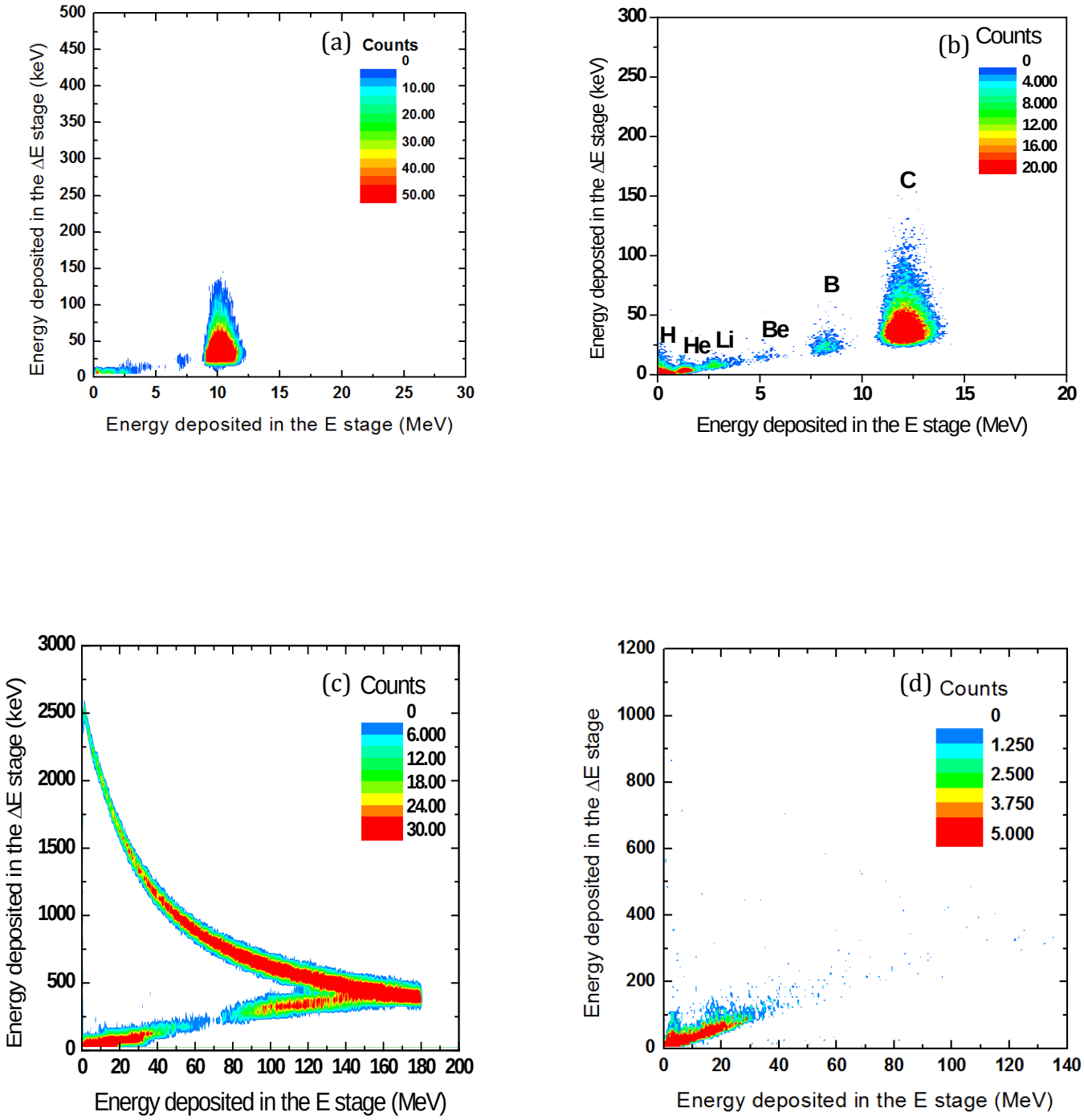

Figure 6.7: ΔE-E scatter plot at phantom depth of (a) 1 cm, (b) 10 cm, (c) 23.5 cm and (d) 26 cm.

The residual energy spectrum acquired in the E stage is of great importance, since the contribution of the primary beam (C) and of its fragments (B, Be, Li, He, H) to the energy spectrum can be assessed individually, as shown in figure 6.8 for the phantom depth of 10 cm.

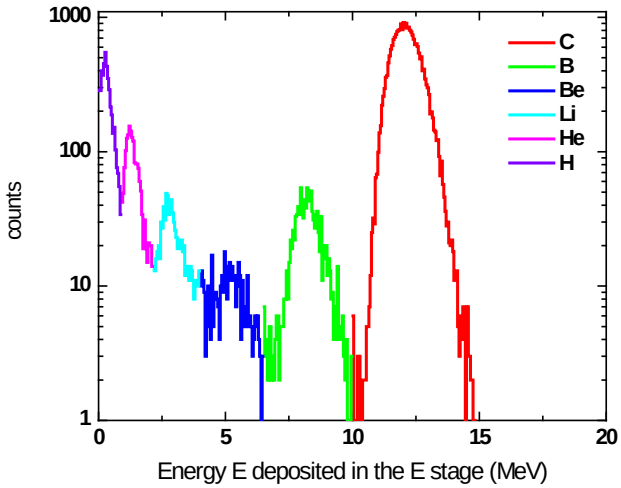

Figure 6.8: Residual energy spectrum acquired by the E stage of the detector at the depth of 10 cm, where the contribution to the energy spectrum of the primary beam and its fragments can be assessed.

The microdosimetric spectra corrected adequately for shape and tissue equivalence that were derived for the simulated phantom depths are shown in figures 6.9 (a) – (d). In the carbon fragment tail shown in figure 6.9 (d), the simulated events are distributed at low lineal energies below 100 keV μm^{-1}. These events refer mainly to protons from fragmentation, since heavier ions cannot observed because of the insufficient statistics obtained in a fairly long computing time.

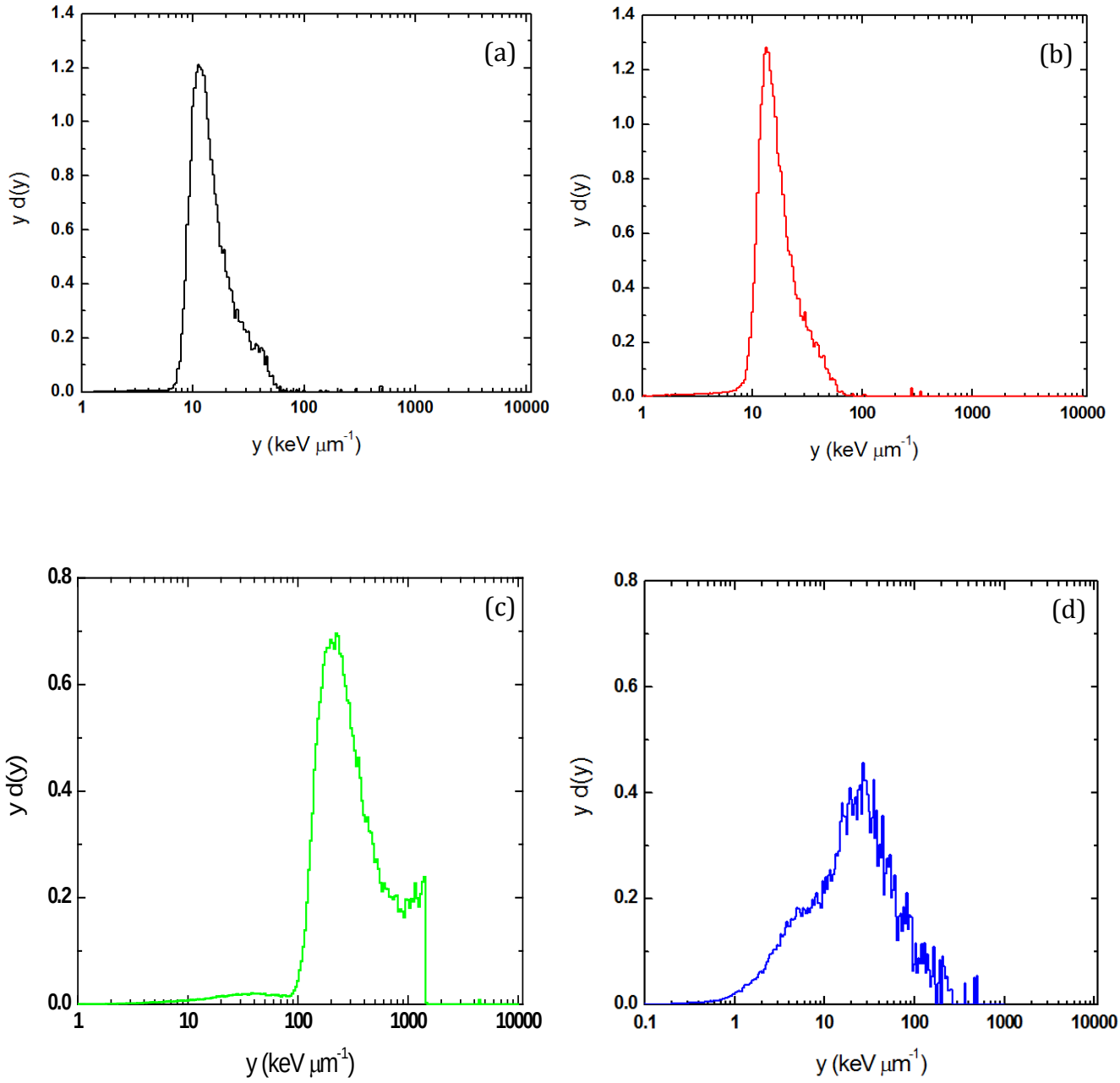

Figure 6.9: Microdosimetric spectrum at a depth of (a) 1 cm (black curve), (b) 10 cm (red curve), 23.5 cm (green curve) and (d) 26 cm (blue curve) inside the phantom.

CHAPTER 7

Primary test of a monolithic silicon telescope with a 70 MeV carbon ion beam

The silicon microdosimeters are in principle intended to be applied for quality assessment of hadron therapy fields, in order to improve the effectiveness of the therapeutic treatment. However, the information that they can provide can be useful in various research activities. In this context, a monolithic silicon microdosimeter was irradiated with a 70 MeV (in total kinetic energy) carbon ion beam in vacuum at the Heavy Ion Accelerator Facility of the Australian National University for an experiment that aims to study the radiobiological effectiveness of a therapeutic carbon ion beam at the distal part of the Bragg peak, with minimal fragment contribution. The measurements were performed with a successor version of a monolithic silicon microdosimeter in vacuum.

This experimental campaign was challenging, since the device was irradiated for the first time and there was a risk of electronics failure due to the vacuum. Preliminary results on the device's response were acquired that consist a solid base for a future more detailed study of its performance.

7.1 The Australian National University Heavy Ion Accelerator Facility

The Heavy Ion Accelerator Facility is located on the Australian National University (ANU) campus in Canberra and it consists of a 15 MV electrostatic accelerator and a superconducting linear accelerator (LINAC). The electrostatic accelerator in stand-alone operation services seven beamlines, plus three more in the LINAC hall. The accelerator is operated by the Department of Nuclear Physics of the ANU. A layout of the acceleration complex is show in figure 7.1 [63].

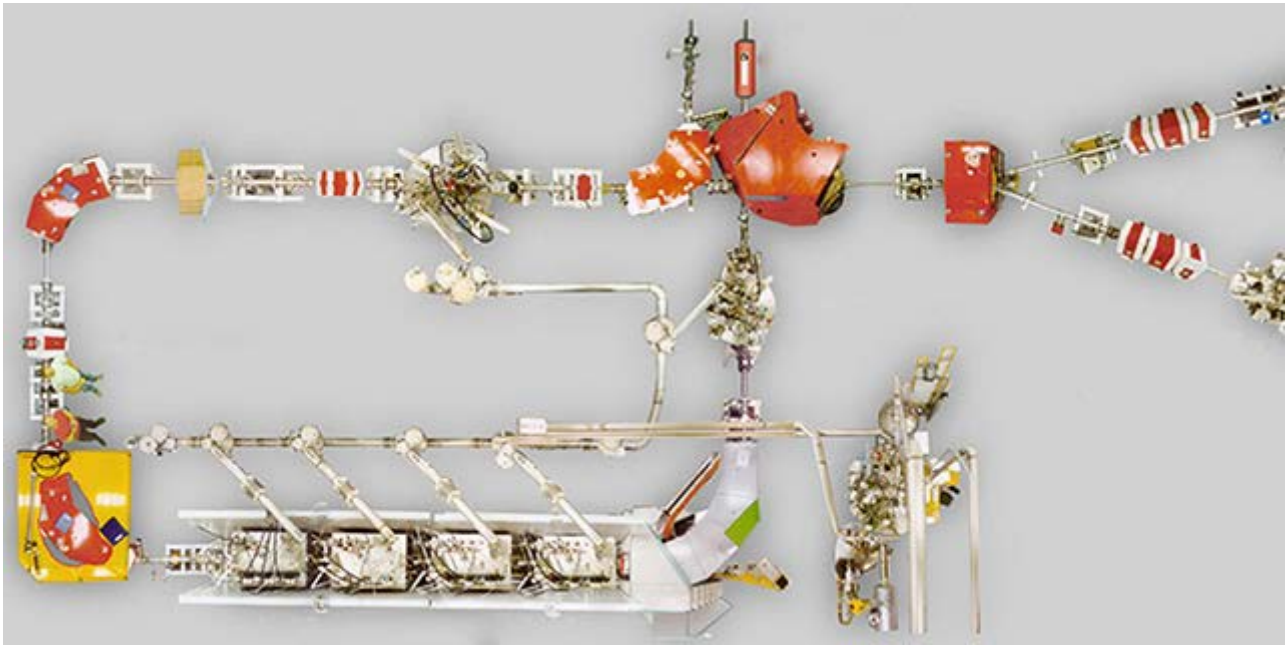

Figure 7.1: A layout of the Heavy Ion Accelerator Facility complex.

7.2 The irradiation set-up

A new experimental model of a monolithic silicon microdosimeter was irradiated with a 70 MeV carbon ion beam. The detector was coupled with a polyethylene converter (about 1 mm in thickness), its sensitive area was collimated by it positions was fixed. Shielding of aluminum foil was placed around the detector and was connected to the measurement ground.

In front of the device a ladder with stacks of mylar foils of different thicknesses (100 μm, 150 μm, 160 μm – 185 μm in steps of 5 μm) was placed and was moved vertically, providing different measurement points across the Bragg peak. The entire detection system was placed inside a vacuum chamber. The left part of figure 7.2 the irradiation setup inside the vacuum chamber and including part of the beam delivery system are shown, while on the right is a picture of the detector from the perspective of the impinging beam.

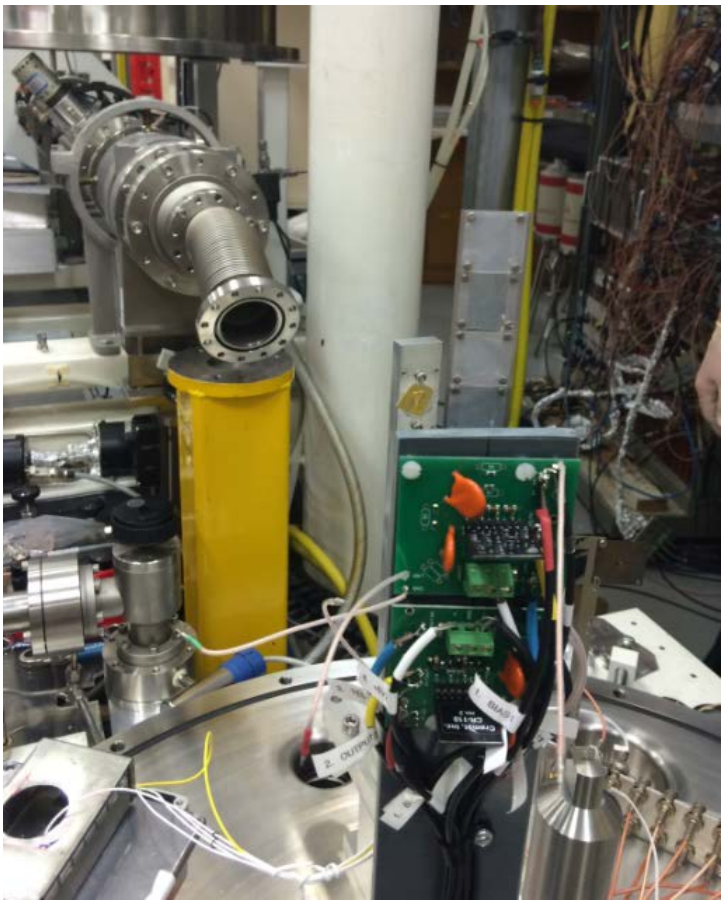

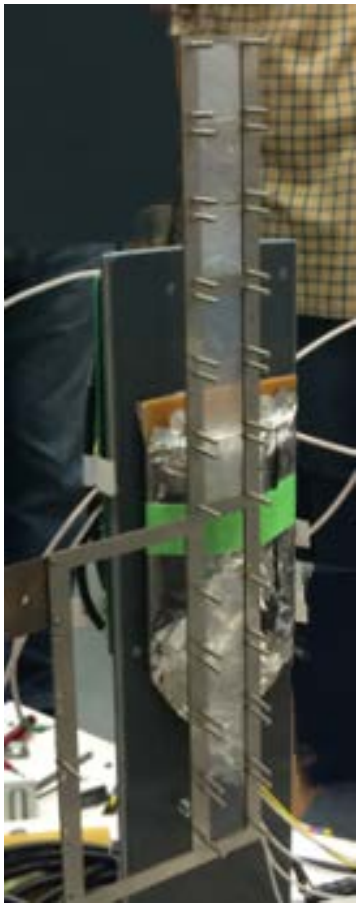

Figure 7.2: Left: A picture of the irradiation set-up. Right: The set-up of the detector in the direction of the beam.

7.3 Experimental results

These sets of measurements consist a primary test of the response of a detector irradiated for the first time and provide useful information on its performance. The energy deposited in the silicon detector of a 70 MeV carbon ion beam, after interacting with mylar foils, for different points along the Bragg peak was measured.

The scatter plots of the energy imparted per event in the ΔE stage versus that deposited the total energy deposited in both ΔE and E stage, together with the analytical response to carbon ions of the monolithic silicon telescope (black curve), for several measurement points are shown in figures 7.3 (a) – (g). Figure 7.3 (a) shows the scatter plot acquired without any mylar foils, thus the total energy deposited is almost the total kinetic energy of the primary beam, as expected. After the addition of the mylar foils, the total energy deposited in the detector is progressively decreasing, due to the interaction of the beam with the mylar foils. The energy lost due to the interaction with the mylar increases with the mylar thickness, as can be observed through figures 7.3 (b) – (g). The plots are scaled accordingly to fully depict the statistics.

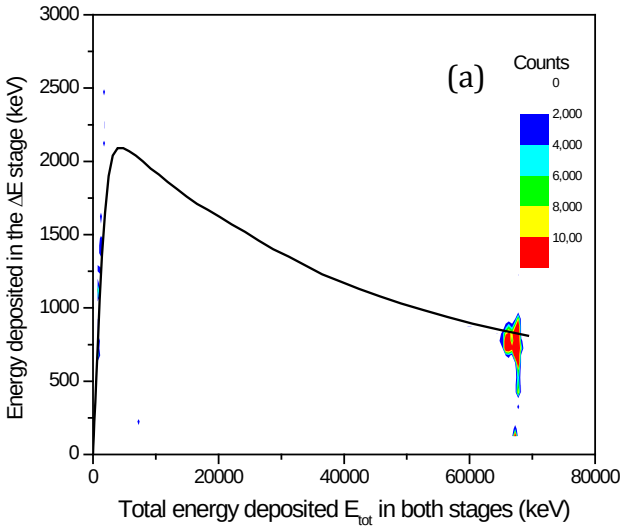
(a)
Counts
0
2,000
4,000
6,000
8,000
10,00
Energy deposited in the ΔE stage (keV)
Total energy deposited E_tot in both stages (keV)
0
500
1000
1500
2000
2500
3000
0
20000
40000
60000
80000

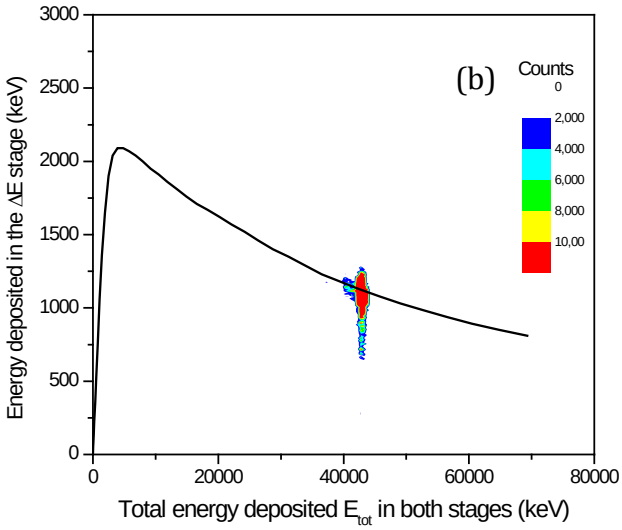
(b)
Counts
0
2,000
4,000
6,000
8,000
10,00
Energy deposited in the ΔE stage (keV)
Total energy deposited E_tot in both stages (keV)
0
500
1000
1500
2000
2500
3000
0
20000
40000
60000
80000

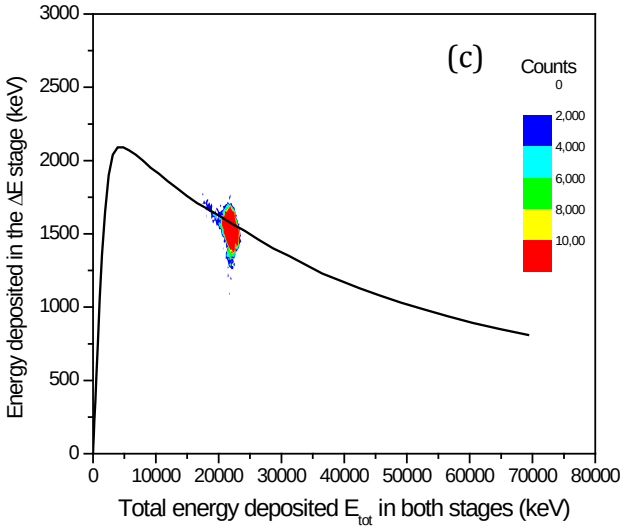
(c)
Counts
0
2,000
4,000
6,000
8,000
10,00
Energy deposited in the ΔE stage (keV)
Total energy deposited E_tot in both stages (keV)
0
500
1000
1500
2000
2500
3000
0
10000
20000
30000
40000
50000
60000
70000
80000

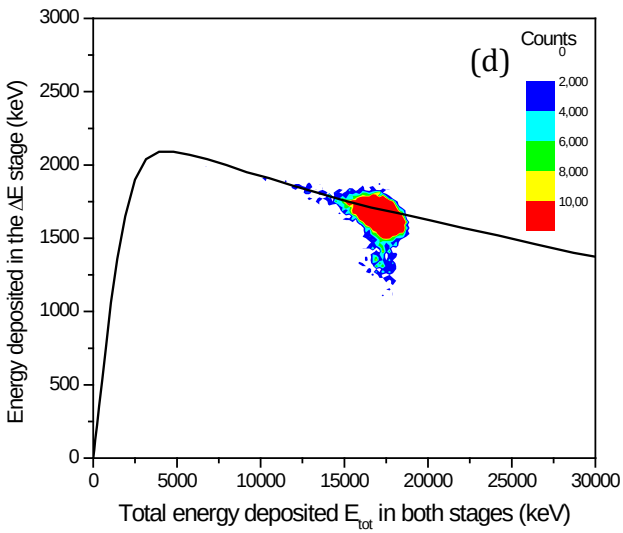
(d)
Counts
0
2,000
4,000
6,000
8,000
10,00
Energy deposited in the ΔE stage (keV)
Total energy deposited E_tot in both stages (keV)
0
500
1000
1500
2000
2500
3000
0
5000
10000
15000
20000
25000
30000

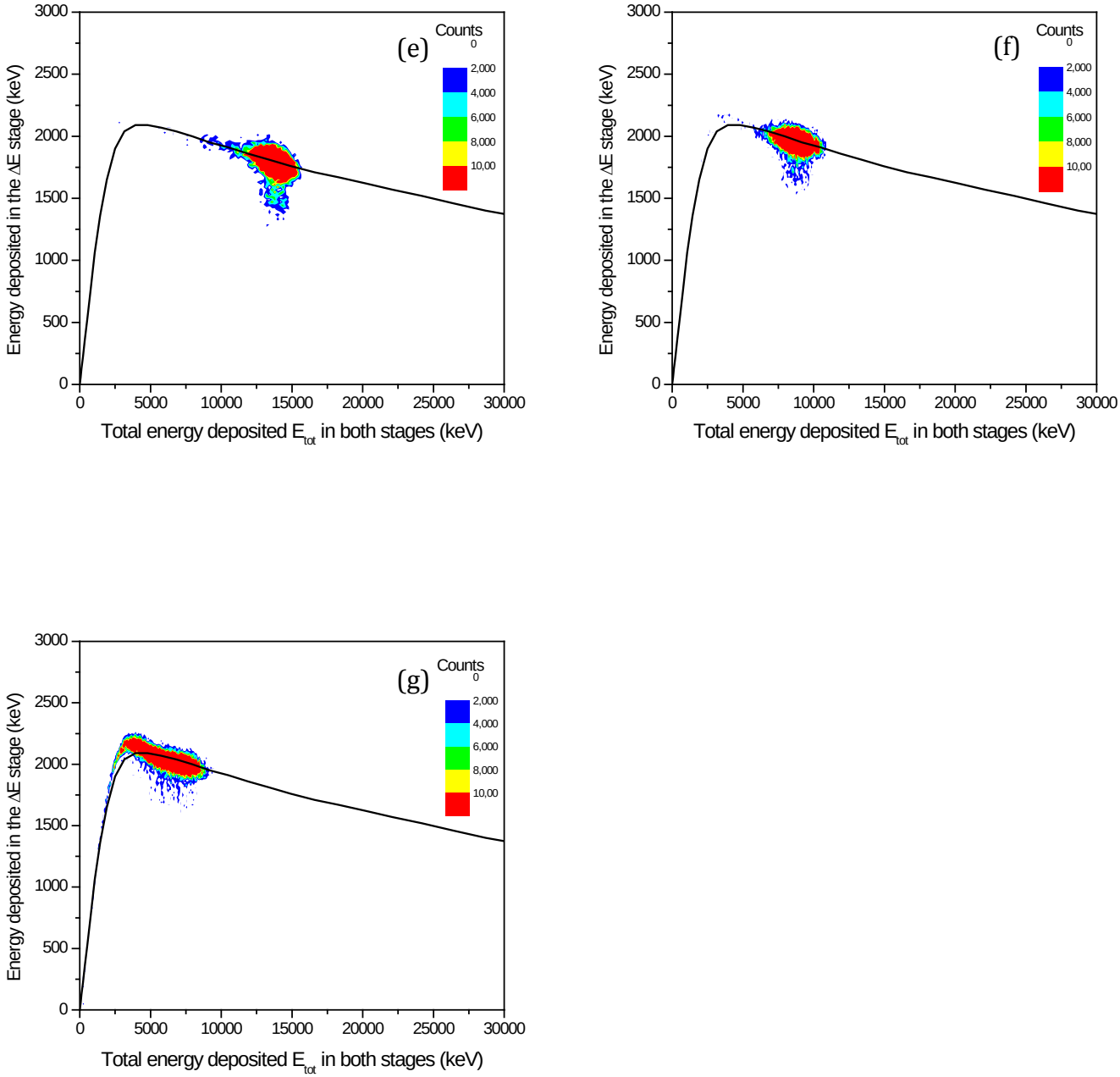

Figure 7.3: ΔE – Etot scatter plot measured with the detector placed behind a mylar foil of (a) 0 µm, (b) 100 µm, (c) 150 µm, (d) 160 µm, (e) 170 µm, (f) 180 µm and (g) 185 µm. The black line is the analytical response of the detector to carbon ions.

The present study investigates if the possibility of assessing the quality of a therapeutic proton beam though microdosimetric measurements with a monolithic silicon telescope that has already been proven can also be extended to carbon ions. To this aim, multiple experimental activities, in addition to numerical studies based on FLUKA Monte Carlo simulations were carried out. Scatter plot and linear energy distributions acquired at different hadron therapy facilities were compared with numerical, experimental and literature data, in order to verify the detector response to the various irradiation fields.

The reproducibility of the results from the irradiation of the SMST at the CATANA facility with a 62 AMeV carbon ion beam is demonstrated through comparison of some common points with the preliminary measurements performed in the past. The microdosimetric profile and the characterization of the irradiation field were completed by summarizing all sets of measurements.

A carbon ion beam of the energy of 290 AMeV was characterized with the use of both MST and SMST at the HIMAC facility. The extensive measurements enabled the comparison of the response of the two detectors to the same field and also the comparison of the microdosimetric profiles of two differently delivered fields (pristine and clinical) of the same energy. The numerical results were compared and found in agreement with the experimental data, confirming the consistency of the results and enhancing the confidence on the detectors' performance in high energy and flux hadron therapy fields.

Preliminary measurements were carried out at the CNAO facility, in order to test the capability of the silicon microdosimeter of reproducing microdosimetric spectra similar to those acquired with a mini-TEPC in carbon ion therapeutic fields. These measurements are among the first microdosimetric measurements performed in therapeutic carbon ion field and the first that are carried out together with the reference detection system. The results of the comparison between the microdosimetric spectra derived with the two detection systems were considered to be satisfactory and the detector capability is confirmed. Minor deviations that occurred could be due to uncertainty in the precision of positioning of the two detectors (their dimensions are of different order of magnitude with the silicon detector being in μm while mini TEPC in mm) and to uncertainties induced by possible geometrical differences related to the chord length distribution in the sensitive volumes. Also, for this particular set of measurements the superiority of the TEPC concerning the minimum detectable energy does not seem to affect the final result. Due to the small number of measuring positions though, it is not safe to draw any conclusions concerning this issue and therefore supplementary measurements are recommended.

In conclusion, the capability of the silicon detectors to acquire microdosimetric spectra similar to those obtained with a reference microdosimeter has been confirmed, especially with the experimental campaign at the CNAO facility where a direct comparison was made. However, all results (including the ones of the mini-TEPC) were carried out at beam currents

about two orders of magnitude lower than clinical ones, due to signal saturation and pile-up effects. Still, the irradiations in such high energy and flux fields provided useful information on the detector's behavior that concerns the charge collection by the pixels guards. These indications require further investigation and could be the subject of future research.

Finally, a primary test of a new version of a monolithic silicon microdosimeter was carried out with a low energy carbon ion beam at the HIAF facility. The outcome of the new detector test, based on the successful execution of the experimental procedure and to the good experimental results was considered to be satisfactory. Nevertheless, a feasibility study is necessary to be conducted in the future and additional irradiations are recommended for a more detailed analysis of the new detector's behavior and performance, especially focusing on the possible impact of the modifications of the new version device might have.

References

[1] Microdosimetey and its applications, *H.H. Rossi, M. Zaider* – Springer (1996), New York.

[2] International Commission on Radiation Units and Measurements, *ICRU Report 16* ICRU (1970), Bethesda, MD.

[3] International Commission on Radiation Units and Measurements, *Microdosimetry (ICRU Report 36)* ICRU (1983), Bethesda, MD.

[4] International Commission on Radiological Protection, *ICRP Publication 103* (2007), Vol. 37, (2-4).

[5] Radiological Use of Fast Protons, *R.R. Wilson* – Radiology (1946), Vol. 47, Issue 5 pp: 487-491.

[6] History of hadrontherapy in the world and Italian developments, *U. Amaldi* – Rivista Medica (2008), Vol. 14, No 1, pp: 7-22.

[7] International Commission on Radiation Units and Measurements, *ICRU Report 33* ICRU (1980), Bethesda, MD.

[8] http://www.orau.org/

[9] Note on the Bragg-Gray Cavity Principle for Measuring Energy Dissipation, *U. Fano* – Radiation Research Society (1954), Vol. 1, No 3, pp: 237-240.

[10] Density effect in dE-dx of fast charged particles traversing various biological materials, *YS. Kim* – Radiation Research (1973), Vol. 56, No 1, pp: 21-27.

[11] Energy distribution in the absorption of radiation, *H.H. Rossi* – Advances in Biological and Medical Physics (1967), Vol. 11, pp: 27-85.

[12] An Assessment of Wall Effects in Microdosimetric Measurements, *A.M. Kellerer* – Radiation Research (1971), Vol. 47, pp: 377-386.

[13] Radiation Detection and Measurement, *G.F. Knoll* – John Wiley & Sons (1971), New York.

[14] Measurement of single event energy deposition spectra at 5 nm to 250 nm simulated site sizes, *P. Kliauga* – Radiation Protection Dosimetry (1990), Vol. 31, No 1/4, pp: 119-123.

[15] Characterization of miniature tissue-equivalent proportional counters for neutron radiotherapy applications, *J. Burmeister, C. Kota, R.L. Maughan, A.J. Walker* – Physics in Medicine and Biology (2002), Vol. 47, pp: 1633-1645.

[16] Mini-TEPCs for Radiation Therapy, *L. De Nardo, V. Cesari, G. Donà, G. Magrin, P. Colautti, V. Conte, G. Tornielli* – Radiation Protection Dosimetry (2004), Vol. 108, No 4 pp: 345-352.

[17] Heavy ion therapy: status and perspectives, *O.Jäkel, D.Schulz-Ertner, C.P. Karger, A. Nikoghosyan, J. Debus* – Technology in Caner Research & Treatment (2003), Vol. 2, No 5.

[18] Significance and implementation of RBE variations in proton beam therapy, *H. Paganetti* – Technology in Cancer Research and Treatment (2003), Vol. 2, pp: 413-26.

[19] Radiotherapy with Beams of Carbon Ions, *U. Amaldi, G. Kraft* - Reports on Progress in Physics (2005), Vol. 68, pp: 1861-1882.

[20] Specification of Carbon Ion Dose at the National Institute of Radiological Sciences (NIRS), *N. Matsufuji, T. Kanai, N. Kanematsu, T. Miyamoto, M. Baba, T. Kamada, H. Kato, S.Yamada, J. Mitzoe, H. Tsujii* - Journal of Radiation Research (2007), Vol. 48, pp: A81-A86.

[21] Sensitivity analysis of the relative biological effectiveness predicted by the local effect model, *T. Friedric., R. Grün., U. Scholz., T. Elsässer, M. Durante., M. Scholz* - Physics in Medicine and Biology (2013), Vol. 58, pp: 6827-49.

[22] The role of microdosimetry in radiotherapy, *A. Wambersie, P. Pihet, H.G. Menzel*- Radiation Protection Dosimetry (1990), Vol. 31, pp: 421-432.

[23] An estimation of relative biological effectiveness of 50 MV bremsstrahlung beams by microdosimetric techniques, *A. Tilikidis, B. Lind, P. Nafstadius, A. Brahme* – Physics in Medicine and Biology (1996), Vol. 41, pp: 55-69.

[24] Biological Weighting Function for RBE Specification of Neutron Therapy Beams. Intercomparison of 9 European Centres, *P. Pihet, H.G. Menzel, R. Schmidt, M. Beauduin, A. Wambersie*- Radiation Protection Dosimetry (1990), Vol. 31, pp: 437-442.

[25] Radiobiological Effectiveness of radiation beams with broad LET spectra: microdosimetric analysis using biological weighting functions, *T. Loncol, V. Cosgrove, J.M. Denis, J. Gueulette, A. Mazal, H.G. Menzel, P. Pihet, R. Sabattier* - Radiation Protection Dosimetry (1994), Vol. 52, pp: 347-352.

[26] Microdosimetry spectra of the Loma Linda proton beam and relative biological effectiveness comparisons, *G. Coutrakon, J. Cortese, A. Ghebremedhin, J. Hubbard, J. Johanning, P. Koss, G. Maudsley, C.R. Slater, C. Zuccarelli*- Medical Physics (1997), Vol. 24, pp: 1499-506.

[27] Microdosimetric investigation at the therapeutic proton beam facility of CATANA, *L. De Nardo, D. Moro, P. Colautti, V. Conte, G. Tornielli, G. Cuttone* - Radiation Protection Dosimetry (2004), Vol. 110, pp: 681-686.

[28] Microdosimetric assessment of Nice therapeutic proton beam Biological Quality, *P. Chauvel, G. Tornielli, J. Herault, P. Colautti, V. Conte, N. Iborra, V. Cesari, L. De Nardo* – Physica Medica (2004), Vol. XX, No. 2, pp:71-77.

[29] Microdosimetric evaluation of the 400 MeV/nucleon carbon beam at HIMAC, *S. Endo, K. Tanaka, M. Ishikawa, M. Hoshi, Y. Onizuka, M. Takada, H. Yamaguchi, N. Hayabuchi, N. Maeda, K. Shizuma* – Medical Physics (2005), Vol. 32, pp: 3843-3848.

[30] Microdosimetric evaluation of secondary particles in a phantom produced by carbon 290 MeV/nucleon ions at HIMAC, *S. Endo, M. Tanaka, Y. Onizuka, K. Takada, N. Maeda, M. Ishikawa, N. Hayabuchi, K. Shizuma, M. Hoshi* – Journal of Radiation Research (2007), Vol. 48, pp: 397-406.

[31] Measurement of microdosimetric spectra produced from a 290 MeV/n Spread Out Bragg Peak carbon beam, *S. Endo, M. Takada, H. Tanaka, Y. Onizuka, K. Tanaka, N. Miyahara, H. Baba, A. Oishi, M. Ishikawa, M. Hoshi, S. Kimura, M. Minematsu, Y. Morimune, Y. Kojima, K. Shizuma* - Radiation Environmental Biophysics (2010), Vol. 49, pp: 469-475.

[32] Microdosimetric measurements in the secondary radiationfield produced in 12C-therapy irradiations, *F. Wissmann, U. Giesen, T. Klages, D. Schardt, G. Martino, C. Sunil* - Radiation Environmental Biophysics (2010), Vol. 49, pp: 331-336.

[33] Microdosimetry at Middle Age: Some Old Experimental Problems and New Aspirations, *F. Wissmann, P. Kliauga* - Radiation Research (1990), Vol. 124, No. 1, pp: S5-S15.

[34] A Comparison of Microdosimetric Measurements with Spherical Proportional Counters and Solid-State Detectors, *J.F. Dicello, H.I. Amols, M. Zaider, G. Tripard* – Radiation Research (1980), Vol. 82, No. 3, pp: 441-453.

[35] Microelectronics and microdosimetry, *J.F. Dicello* – Nuclear Instruments and Methods in Physics Research (1987), Vol. B24/25, pp: 1044-1049.

[36] Microdosimetric counters based on semiconductors detectors, *M. Orlic, V. Lazarevic, F. Boreli* – Radiation Protection Dosimetry (1989), Vol. 29, pp: 21-22.

[37] Performance of PIN photodiode in microdosimetry, *A. Kadachi, A. Waheed, and M. Obeid* – Health Physics (1994), Vol. 66, pp: 577-580.

[38] Solid state microdosimetry, *P.D. Bradley, A.B. Rosenfeld, M. Zaider* – Nuclear Instruments and Methods in Physics Research B (2001), Vol. 184, pp: 135-157.

[39] New silicon detector for microdosimetry applications in proton therapy, *A.B. Rosenfeld, P. Bradley, I. Corneluis, G. Kaplan, B. Allen, J. Flanz, M. Goitein, A.V. Meerbeeck, J. Schubert, J. Bailey, Y. Tabkada, A. Maruashi, Y. Hayakawa* – IEEE Transactions on Nuclear Science (2000), Vol. 47, pp: 1386-1394.

[40] Solid state microdosimetry in hadron therapy, *A.B. Rosenfeld et al* – Radiation Protection Dosimetry (2002), Vol. 101, pp: 431-434.

[41] A Solid State Microdosimeter based on a Monolithic Silicon Telescope, *S. Agosteo, P. Colautti, A. Fazzi, D. Moro, A. Pola* - Radiation Protection Dosimetry (2006), Vol. 122, pp: 382-386.

[42] Silicon Microdosimetry, *S. Agosteo, , A. Pola* - Radiation Protection Dosimetry (2010), Vol. 143, pp: 409-415.

[43] Considerations on the Random Traversal of Convex Bodies and Solutions for General Cylinders, *A.M. Kellerer* - Radiation Research (1971), Vol. 47, No. 2, pp: 359-376.

[44] Criteria for the Equivalence of Spherical and Cylindrical Proportional Counters in Microdosimetry, *A.M. Kellerer* - Radiation Research (1981), Vol. 86, No. 2, pp: 277-286.

[45] A Field-funneling Effect on the Collection of Alpha-Particle-Generated Carriers in Silicon Devices, *C.M. Hsieh, P.C. Murley, R.R. O'Brien* – IEEE Electron Device Letter (1981), Vol.2, No. 4, pp: 103-105.

[46] A monolithic silicon telescope, *G. Cardella, F. Amorini, M. Cabibbo, A. Di Pietro, G. Fallica, G. Franzò, P. Figuera, S. Li, A. Musumarra, M. Papa, G. Pappalardo, G. Percolla, F. Priolo, V. Privitera, F. Rizzo, S. Tudisco* – Nuclear Instruments and Methods A (1996), Vol. 378, pp: 262-266.

[47] A new large area monolithic silicon telescope, *S. Tudisco, F. Amorini, M. Cabibbo, G. Cardella, G. De Geronimo, A. Di Pietro, G. Fallica, P. Figuera, A. Musumarra, M. Papa, G. Pappalardo, F. Rizzo, G. Valvo* – Nuclear Instruments and Methods A (1996), Vol. 426, pp: 436-445.

[48] A Pixelated Silicon Telescope for Solid State Microdosimeter, *S. Agosteo, P.G. Fallica, A. Fazzi, M.V. Introini, A. Pola, G. Valvo* – Radiation Measurements (2008), Vol. 43, pp: 585-589.

[49] Test of the ΔE/E silicon microdosimeter at the CATANA facility, *A. Fazzi, S. Agosteo, A. Pola, M.V. Introini, V. Varoli* – IEEE Nuclear Science Symposium, Orlando (FL) (2009), Conference Record.

[50] Feasibility study of radiation quality assessment with a monolithic silicon telescope: Irradiations with 62 AMeV carbon ions at LNS-INFN, *S. Agosteo, G.A.P. Cirrone, G. D'Angelo, A. Fazzi, M.V. Introini, A. Pola* - Radiation Measurements (2011), Vol. 46, Issue 12, pp: 1534–1538.

[51] http://www.lnl.infn.it/index.php/it/

[52] CATANA protontherapy facility: The state of art of clinical and dosimetric experience, *G. Cuttone, G.A.P. Cirrone, G. Di Franco, V. La Monaca, S. Lo Nigro, J. Ott, S. Pittera, G. Privitera, L. Raffaele, A. Reibaldi, F. Romano, M.G. Sabini, V. Salamone, M. Sanfilippo, C. Spatola, L.M. Valastro* – The European Physical Journal Plus (2011), Vol. 126:65.

[53] Proton therapy detector studies under the experience gained at the CATANA facility, *G. Cuttone, G.A.P. Cirrone, F. Di Rosa, P.A. Lojacono, S. Lo Nigro, C. Marino, V. Mongelli, I.V. Patti, S. Pittera, L. Raffaele, G. Russo, M.G. Sabini, V. Salamone, L.M. Valastrod* – Nuclear Physics B - Proceedings Supplements (2007) Vol. 172, pp: 79–83.

[54] Analytical model for a monolithic silicon telescope – Response function of the E stage, *S. Agosteo, A. Pola* – Radiation Measurements (2008) Vol. 43, pp: 1487–1492.

[55] Heavy Ion Medical Accelerator in Chiba (HIMAC), *K. Sato et al* – Particle Accelerators (1990), Vol. 33, pp. 147-152.

[56] Cancer Treatment by Charged Particles – Carbon Ion Radiotherapy, *T. Murakami* –Taiwan Summer School lectures 2012.

[57] Biophysical characteristics of HIMAC clinical irradiation system for heavy-ion radiation therapy, *T. Kanai et al* – Int. J. Radiation Oncology Biol. Phys. (1999), Vol. 44, No. 1, pp. 201-210.

[58] FLUKA: a multi-particle transport code, *A. Ferrari*, *P.R. Sala*, *A. Fassò*, *and J. Ranft* – CERN 2005-10 (2005), INFN/TC_05/11, SLAC-R-773.

[59] The FLUKA Code: Developments and Challenges for High Energy and Medical Applications, *T.T. Böhlen*, *F. Cerutti*, *M.P.W. Chin*, *A. Fassò*, *A. Ferrari*, *P.G. Ortega*, *A. Mairani*, *P.R. Sala*, *G. Smirnov and V. Vlachoudis* – Nuclear Data Sheets 120 (2014), pp. 211-214.

[60] http://www.cnao.it/

[61] Status report on the "Centro Nazionale di Adroterapia Oncologica" (CNAO) - *CNAO collaboration,* Genoa, Italy (2008), Proceedings of EPAC08.

[62] Performances of the scanning system for the CNAO center of oncological hadron therapy - *S. Giordanengo, M. Donetti, F. Marchetto, A. Ansarinejad, A. Attili, F. Bourhaleb, F. Burini, R. Cirio, P. Fabbricatore, F. Voelker, M. A. Garella, M. Incurvati, V. Monaco, J.* ***Pardo****, C. Peroni, G. Russo, R. Sacchi, G. Taddia and A. Zampier*, Nucl. Instrum. Methods Phys. Res. (2010), Sect. A 613, pp. 317–322.

[63] http://physics.anu.edu.au/